WARWICK
THE UNIVERSITY OF WARWICK

Manuscript version: Author's Accepted Manuscript
The version presented in WRAP is the author's accepted manuscript and may differ from the published version or Version of Record.

Persistent WRAP URL:
http://wrap.warwick.ac.uk/165420

How to cite:
The repository item page linked to above, will contain details on accessing citation guidance from the publisher.

Copyright and reuse:
The Warwick Research Archive Portal (WRAP) makes this work of researchers of the University of Warwick available open access under the following conditions.

This article is made available under the Creative Commons Attribution 4.0 International license (CC BY 4.0) and may be reused according to the conditions of the license. For more details see: http://creativecommons.org/licenses/by/4.0/.

Publisher's statement:
Please refer to the repository item page, publisher's statement section, for further information.

For more information, please contact the WRAP Team at: wrap@warwick.ac.uk

warwick.ac.uk/lib-publications

Using positional information to provide context for biological image analysis with MorphoGraphX 2.0

Soeren Strauss[2], Adam Runions[2,7], Brendan Lane[1,2], Dennis Eschweiler[5], Namrata Bajpai[2], Nicola Trozzi[1,2], Anne-Lise Routier-Kierzkowska[3], Saiko Yoshida[2], Sylvia Rodrigues da Silveira[3], Athul Vijayan[4], Rachele Tofanelli[4], Mateusz Majda[1,2], Emillie Echevin[3], Constance Le Gloanec[3], Hana Bertrand-Rakusova[3], Milad Adibi[2], Kay Schneitz[4], George Bassel[6], Daniel Kierzkowski[3], Johannes Stegmaier[5], Miltos Tsiantis[2], Richard S. Smith[1,2*]

[1] John Innes Centre, Norwich Research Park, Norwich, NR4 7UH, UK.

[2] Max Planck Institute for Plant Breeding Research, Carl-von-Linne-Weg 10, Cologne 50829, Germany.

[3] MIRBV, Department of Biological Sciences, University of Montreal, 4101 Sherbrooke Est, Montréal H1X 2B2, QC, Canada.

[4] Plant Developmental Biology, TUM School of Life Sciences, Technical University of Munich, Freising, Germany.

[5] Institute of Imaging and Computer Vision, RWTH Aachen University, Aachen, Germany.

[6] School of Life Sciences, University of Warwick, Coventry, CV4 7AL, UK.

[7] Current address: Department of Computer Science, University of Calgary, Calgary, Alberta, T2N 1N4, Canada.

[*] Correspondence: Richard.Smith@jic.ac.uk

Abstract

Positional information is a central concept in developmental biology. In developing organs, positional information can be idealized as a local coordinate system that arises from morphogen gradients controlled by organizers at key locations. This offers a plausible mechanism for the integration of the molecular networks operating in individual cells into the spatially-coordinated multicellular responses necessary for the organization of emergent forms. Understanding how positional cues guide morphogenesis requires the quantification of gene expression and growth dynamics in the context of their underlying coordinate systems. Here we present recent advances in the MorphoGraphX software (Barbier de Reuille et al., 2015) that implement a generalized framework to annotate developing organs with local coordinate systems. These coordinate systems introduce an organ-centric spatial context to microscopy data, allowing gene expression and growth to be quantified and compared in the context of the positional information thought to control them.

Introduction

Many aspect of animal morphogenesis are thought to be controlled by positional information (Wolpert, 1969), where cells can sense their position in a developing organ and respond accordingly. This phenomenon may be even more pervasive in plants, as cells cannot relocate within organs, and must decide their fate based on their location. For example, root morphogenesis appears to be controlled by an organizing center at the root tip that provides founder cells and positional information to the growing structure (Scheres et al., 2002). Ablation of cortical cell initials in the root meristem causes the neighboring pericycle cells to divide and fill the available space, subsequently adopting the fate associated to their new location (C. van den Berg et al., 1995). A similar effect has been demonstrated for a variety of cell types in the *Arabidopsis* root (Marhava et al., 2019). In leaves, development is thought to be coordinated by polarity fields oriented from leaf base to tip (Kierzkowski et al., 2019; Kuchen et al., 2012). Over time organs can initiate new growth axes, such as when serrations or leaflets develop in more complex leaves (Barkoulas et al., 2008; Kierzkowski et al., 2019), or lateral roots emerge from the primary root (Scheres et al., 2002). In these cases information from several organizers must be integrated to direct cell response.

To understand how positional information controls morphogenesis, it is necessary to quantify cell shape, gene expression and morphogen concentration changes over time, preferably at the cellular level. This information then needs to be related to its position relative to the organizers controlling development within the organ. As computational power and imaging methods improve, new software packages for cell segmentation and lineage tracking are being developed (Sommer et al., 2011; Stegmaier et al., 2016), including many specialized for plants (Barbier de Reuille et al., 2015; Eschweiler et al., 2019; Fernandez et al., 2010; Schmidt et al., 2014; Wolny et al., 2020). This progress has enabled the segmentation of time-lapse data at increasingly higher resolution and throughput (Hervieux et al., 2016; Kierzkowski et al., 2019; Sapala et al., 2018; Willis et al., 2016). Although this increase in data volume offers tremendous potential to understand how genes control form, the analysis of geometric data from thousands of cells is non trivial. Information about a cell's shape, gene expression and growth directions is of limited value when the cell's spatial context within the developing organ is unknown.

MorphoGraphX is a computer software platform that is specialized for image processing on surface layers of cells (Barbier de Reuille et al., 2015). It has proven especially useful for the analysis of confocal microscopy images from time-lapse data in order to quantify the cellular level dynamics of growth, cell division and gene expression (e.g. Bringmann & Bergmann, 2017; Feng et al., 2018; Hervieux et al., 2016; Hong et al., 2016; Kierzkowski et al., 2019; Louveaux et al., 2016; Sapala et al., 2018; Scheuring et al., 2016; Tsugawa et al., 2017; Vlad et al., 2014; Zhang et al., 2020; Zhu et al., 2020; Fridman et al., 2021). Key to the approach taken in the software is the representation of cell layers as curved, triangulated surface meshes that capture the overall 3D shape of organs, which retains much of the simplicity of 2D segmentation and lineage tracking. These "2.5D" images contain the geometry of the sample at two scales. The global shape of the organ is captured by the mesh's geometry, while a cellular-scale representation is obtained from the confocal signal projected onto the mesh, which is segmented to extract the shape of individual cells on the surface (Fig 1A-C). When combined with time-lapse data acquisition and cell lineage tracking, MorphoGraphX allows cell growth and its relationship to gene expression to be quantified (Fig 1D, E; Kierzkowski et al., 2019; Sapala et al., 2018; Vlad et al., 2014). In addition to cell surface analysis, MorphoGraphX also supports the creation and analysis of full 3D meshes with volumetric cells (Fig 1S1; Vijayan et al., 2021). Here we describe new methods we have developed in MorphoGraphX to understand these data by additionally

annotating cells with positional information. Not unlike the annotation of sequence data, this allows cellular data to be given spatial context, and a frame of reference within the organ relative to its developmental axes and the organizers instructing morphogenesis.

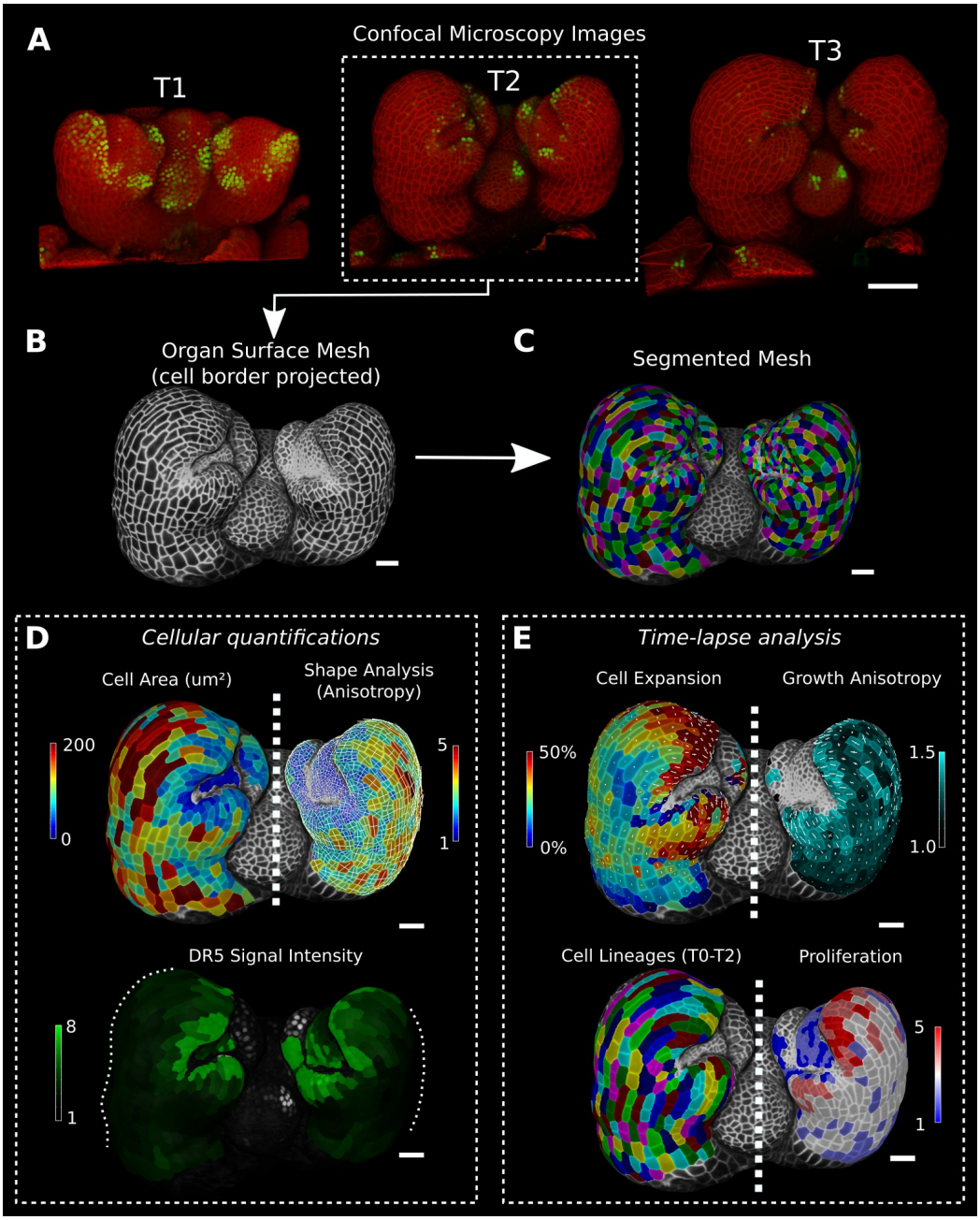

Figure 1: Cellular segmentation and basic quantifications supported by MorphoGraphX demonstrated by using a time-lapse series of an *A. thaliana* flower meristem. (A) Multi-channel confocal microscopy images with a cell wall signal (red) and DR5 marker signal (green). Shown are the last 3 time points (T1-T3) of a 4-image series (T0-T3). (B-C) Extracted surface mesh of T2. Cell wall signal near the surface was projected onto the curved mesh to enable the creation of the cellular segmentation in (C). The segmented meshes provide the base for further analysis within MorphoGraphX as shown in (D) and (E). (D) Top: MorphoGraphX allows the quantification of cellular properties such as cell area and shape anisotropy (shown as heat maps). The white axes show the max and min axes of the cells. Bottom: Heat map of the quantification

of the DR5 marker signal (arbitrary units) projected onto the cell surface mesh. (E) When cell lineages are known, time-lapse data can be analyzed. Top: Heat maps of areal growth and growth anisotropy (computed from T1 to T2). The white lines inside the cells depict the principal directions of growth. Bottom: Visualization of the cell lineages from T0 to T2 and a heat map of cellular proliferation (number of daughter cells). Scale bars: (A) 50µm; (B - E) 20µm. See also user guide sections 1-15 and tutorial videos S1 and S2 available at **https://doi.org/10.5061/dryad.m905qfv1r**.

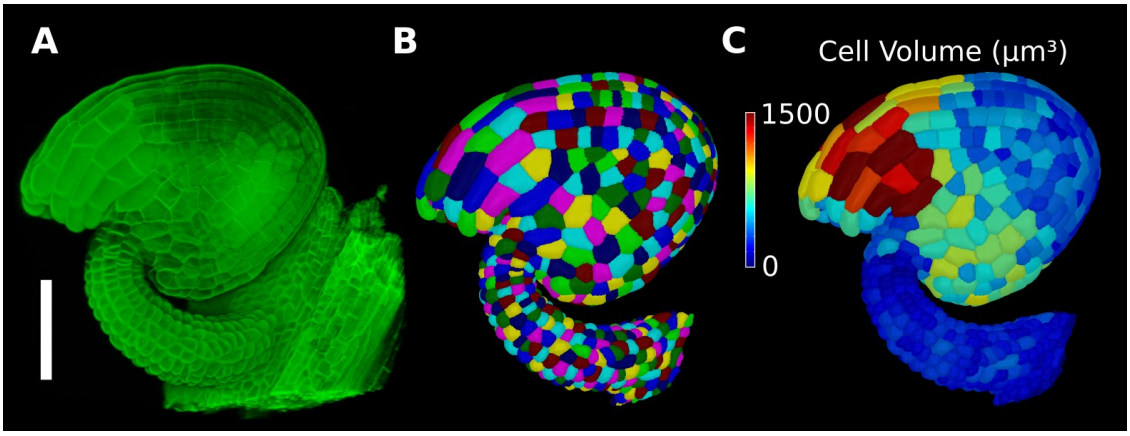

Figure 1-figure supplement 1: Basic 3D analysis using MorphoGraphX demonstrated using an *Arabidopsis* ovule.
(A) Confocal microscopy image with cell wall staining. (B) Segmented mesh with volumetric cells. (C) The segmented mesh allows cellular geometry to be quantified. Shown is a heat map of cell volumes. Scale bar: 50µm. See also user guide sections 20-21 and tutorial video S6 available at https://doi.org/10.5061/dryad.m905qfv1r.

Results

Most workflows in MorphoGraphX begin by converting 3D image stacks into meshes of 2.5D or 3D cellular segmentations, which are created directly on voxels in the case of 3D segmentation, or on surface meshes in the case of 2.5D data (Fig 1A-C; Fig 1S1A, B). Recent advances in voxel classification with convolutional neural networks (CNNs) for cell boundary prediction can improve input images and the resulting segmentation (Eschweiler et al., 2019, 2021; Wolny et al., 2020), especially for 3D segmentations. Although a selection of these and other image de-noising and pre-processing tools are available directly within MorphoGraphX, it is also possible to pre-process and/or segment 3D images in other software, and import them into MorphoGraphX for further analysis. After the initial segmentation, cellular features can be quantified, such as cell area, shape and gene expression for single time points, or cell proliferation and growth for time-lapse data (Fig 1D, E). These data can then be annotated with positional information to aid the understanding of the development of the organism under study. Even with deep learning techniques, image quality needs to be very high for full 3D segmentation, and this is often not possible with live imaged data. By enabling image processing on 2.5D surface images, MorphoGraphX can be used in many systems on live imaged data where full 3D segmentation is currently not possible (Hervieux et al., 2016; Kierzkowski et al., 2019; Sapala et al., 2018; Silveira et al., 2022; Vlad et al., 2014). Annotation with coordinate systems can further reduce image quality requirements in cases where growth along a single dimension is required (Liu et al., 2022).

Defining coordinates within an organ

The simplest method to provide positional information for the cells in a sample is by aligning the sample with a set of 3D coordinate axes (Fig 2A). For example, a developing root meristem can be aligned and positioned such that the organizing quiescent center is at the origin with the Y-axis increasing in the longitudinal direction of the root. Provided the sample is reasonably straight, this allows cellular measures to be compared with their distance from the quiescent center (Fig 2B).

However, for curved organs significant errors will occur, especially in more distal regions, further from the origin. In this case, the central axis can be defined by a curved line which conforms to the curvature of the organ (Fig 2C; Schmidt et al.,

2014; Montenegro-Johnson et al., 2015). In MorphoGraphX, this line can be represented by a Bezier spline (Bézier, 1968) with control points positioned using either interactive manipulation, or automatically from a selected file of cells. Distance can then be calculated along the line, and transferred to cells in the cross section perpendicular to the line (Fig 2C). MorphoGraphX also allows a 2D Bezier surface to be positioned next to or within a sample, enabling two directions to be aligned with the natural curvature of the sample.

Placing the Bezier curve or surface to curved organs with more complex shape is challenging. An alternative method is to select one or more cells at a reference position, and calculate the distance relative to the selection (Fig 2D; Video 1). This offers an easy method to create a distance field, and greatly increases the variety of organs that can be accommodated. The distance is determined by computing the shortest path along cells through the tissue, causing it to naturally follow the curvature of the organ.

Once cells have been annotated with positional information, it can be used for the analysis of cell-level data, such as growth, cell proliferation, cell shape and gene expression. Using the distance measure to define the proximal-distal axis on an *Arabidopsis* sepal (Fig 2D), geometric measures can be plotted against the local coordinate system. In Fig 2F cell area extension was plotted against distance from the base of the sepal. On the full 7 day sepal time-lapse shown in Fig 2S1 (Hervieux et al., 2016), initially growth is predominantly located at the distal parts of the organ, followed by the progressive displacement of the high growth zone towards the base of the sepal (Fig 2S1A). By time point 6, the growth has slowed and become more uniform as the organ differentiates. Proliferation is initially more uniform, but otherwise follows a pattern similar to growth, progressing basally as the organ matures (Fig 2S1B). The data can be indexed by position from the base of the sepal and plotted, showing how growth and proliferation vary along the proximal-distal developmental axis as a percentage of the total sepal length (Fig 2S1D, E). It can be seen in the graphs that although the sepal appears to undergo a similar growth arrest starting at the tip as the *Arabidopsis* leaf, there are subtle differences. The growth in the early stages is more distal in the sepal, along with the proliferation, and the zone of higher growth moves towards the base as the sepal develops. This is in contrast to the *Arabidopsis* leaf where the growth and proliferation zones remain relatively fixed with respect to the total leaf length (cf. Fig 1K, M; Kierzkowski et al., 2019). The use of relative coordinates also makes it possible to pool data from multiple samples (Vijayan et al., 2021; Zhang et al.,

2020) and to compare data from different genotypes (Kierzkowski et al., 2019; Montenegro-Johnson et al., 2019; Zhang et al., 2020).

Deriving directions from organ coordinates

In addition to scalar information such as areal growth rate or cell volume, MorphoGraphX can also quantify directional information, such as the Principal Directions of Growth (PDGs) that represent the maximal and minimal directions of growth for each cell (Fig 3A-C). A common problem with the interpretation of such directional information is the tendency for directions to be locally heterogeneous when growth is nearly isotropic. This happens because the maximal and minimal growth amounts are almost the same, and the displayed directions become arbitrary, and heavily influenced by noise. This can make the comparison of growth directions between neighboring cells difficult. A more informative approach is to look at growth with respect to the directions of the developmental axes. This can be done by first setting up an axis defining the positional information for the leaf, for example by using the previously introduced distance field (Fig 2D; 3B). The growth directions are then projected onto this developmental axis, and separated into components that are parallel (Fig 3D) and perpendicular (Fig 3E) to the axis. Using this method on the *A. thaliana* leaf primordium different developmental zones with varying growth rates along the proximal-distal (P-D) and medial-lateral (M-L) axis can be revealed (Fig 3C-E): While the area extension differs greatly in midrib/petiole (low) and leaf blade cells (high), it can be seen that those differences mainly follow from the M-L growth rate, whereas the P-D growth map is more similar in these domains. Moreover, an increase in M-L growth around the forming serration can be seen, separating it from the surrounding leaf blade cells which show less growth along this direction (Fig 3E). From the original PDG visualization it is not immediately apparent that the varying M-L growth is the main cause for the differences in the domains (Fig 3C).

Another benefit of looking at PDGs in the context of a local coordinate system is that it can provide a more direct comparison to the outputs of computational simulations. Developmental models of emergent organ shape often use morphogens that are thought to specifically control growth in parallel and perpendicular to a developmental axis (Kierzkowski et al., 2019; Kuchen et al., 2012; Whitewoods et al., 2020). By projecting the PDGs onto this axis, it is possible to directly compare model growth rates in the different directions to experiments. Since MorphoGraphX can load a wide variety of mesh formats, this allows the direct comparison of similar quantifications made on templates extracted from model simulations from various sources.

Figure 3F-K shows a similar growth quantification for the tomato meristem (Kierzkowski et al., 2012), where local organ coordinates were created by using cell distance measures around each emerging leaf primordium with directions pointing towards (radial) and around (circumferential) their respective center. In addition to growth, the signal intensity of the auxin reporter DR5 was quantified in the same sample, allowing a direct comparison to auxin signaling levels and cellular growth. For both primordia we found radial growth to have a high negative correlation with DR5 signal intensity. Figure 3J shows that the growth (red) peaks on the abaxial side of the emerging primordium, whereas the DR5 signal (blue) is higher on the adaxial side. Circumferential growth was more or less constant. The DR5 maximum tends to be on the adaxial side of the initiating leaf, whereas growth is much higher on the opposing abaxial side. This supports the idea that auxin acts as a trigger for primordium initiation (Reinhardt et al., 2003; Smith et al., 2006), rather than via controlling growth rates directly.

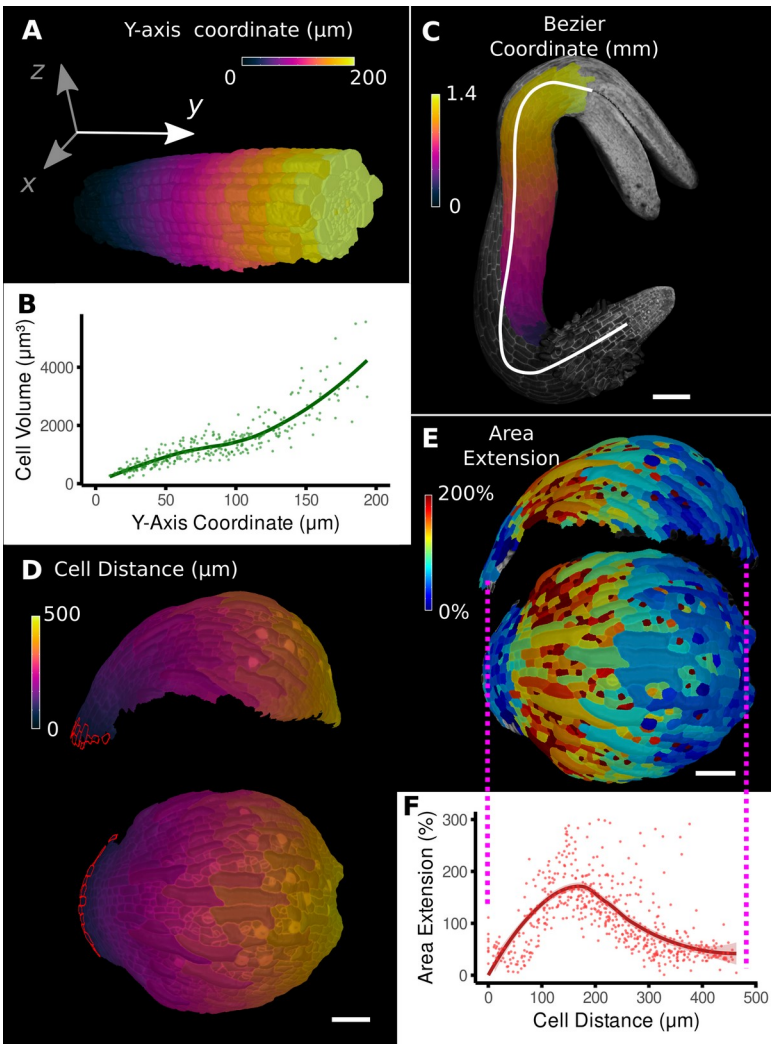

Figure 2: Methods to define positional information and their application to data analysis in plant organs. (A) Y-axis aligned *A. thaliana* root. The cells are colored according to the y-coordinate of their centroid position. (B) Plot of cell volumes of epidermis cells of the root in (A) along the y-axis with a fitted trend line. (C) Seedling of *A. thaliana* with a surface segmentation of the epidermis. A manually defined Bezier curve (white) allows the assignment of accurate cell coordinates along a curved organ axis. (D) Side and top view of an *A. thaliana* sepal with a proximal-distal (PD) axis heat coloring. The cell coordinates were assigned by computing the distance to manually selected cells (outlined in red) at the organ base. This method allows organ coordinates to be assigned in highly curved tissues. (E) Side and top view of (D) with a heat map coloring based on cellular growth to the next time point. (F) Plot summarizing the growth data of (E) using the PD-axis coordinates from (D). See Figure 2-figure supplement 1 for the analysis of the complete time-lapse series. Scale bars: (A) 20 µm; (C) 100 µm; (D, E) 50 µm. See also user guide section 23 “Organ-centric coordinate systems” and tutorial video S3 available at https://doi.org/10.5061/dryad.m905qfv1r.

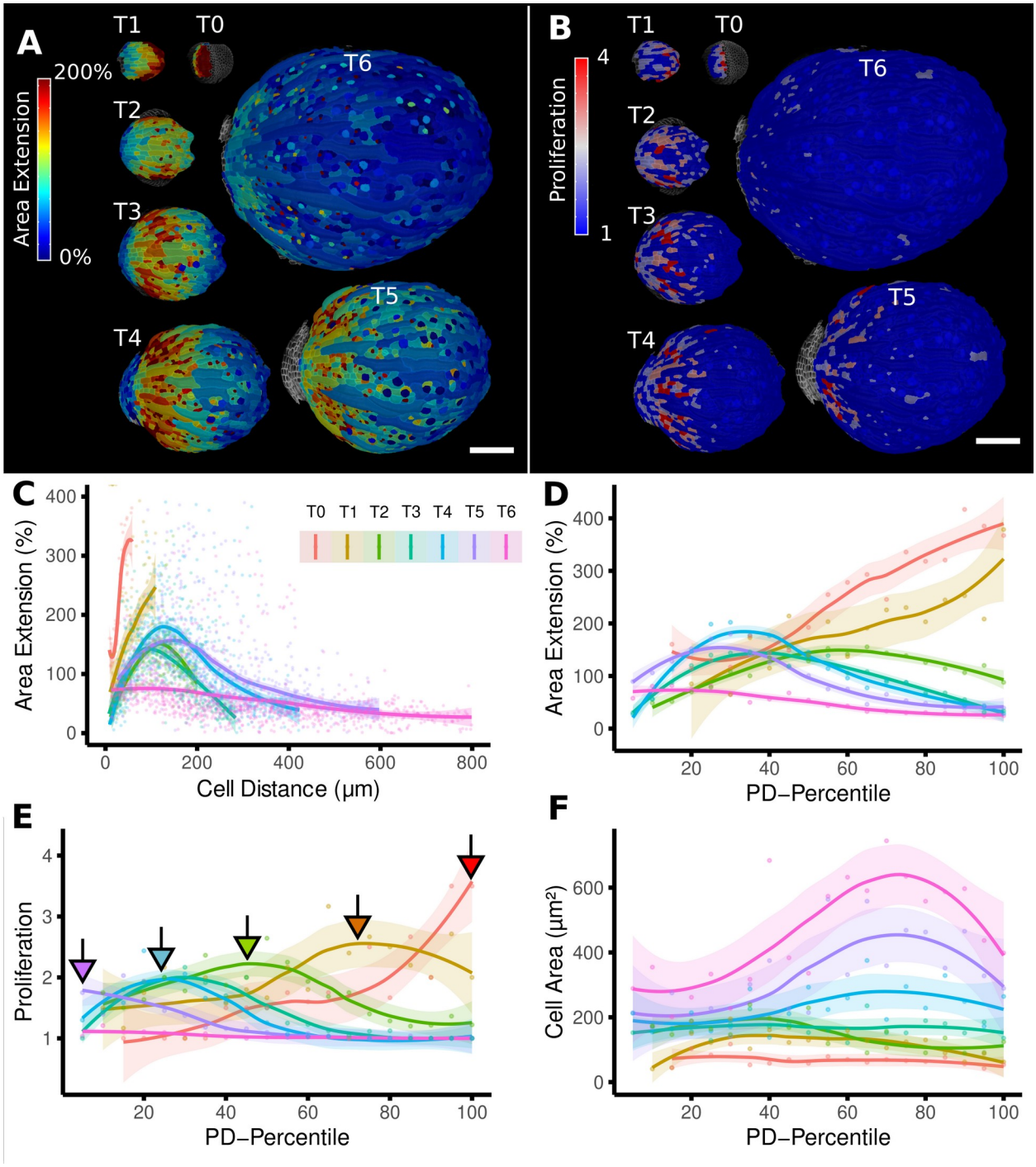

Figure 2-figure supplement 1: From cellular resolution heat maps to a global analysis of *A. thaliana* sepal development using organ-centric coordinates. (A-B) Heat maps of cell area extension (A) and cell proliferation (B) for each time point (visualized on the earlier point). (C) Plot of the heat map data from (A) vs the distance of cells to the base of the organ (see also Fig

2D). The distance of the maximum of the growth zone from the base or the organ is relatively constant. However, organ length is increases about 10x between the first and last time points, making a comparison of the different curves difficult. (D-F) When plotting the same data with normalized cell distance values averaged using 20 bins along the proximal-distal axis it becomes more apparent that the growth zone moves from the proximal to the distal regions over the course of development (D). The trend of lower and more proximal maxima (highlighted with arrows) is even clearer when proliferation is plotted in the same way (E). (F) Cell area data plotted as in (D) and (E). Average cell areas increase mainly at the distal end during later time points. Scale bars: (A, B) 100 μm.

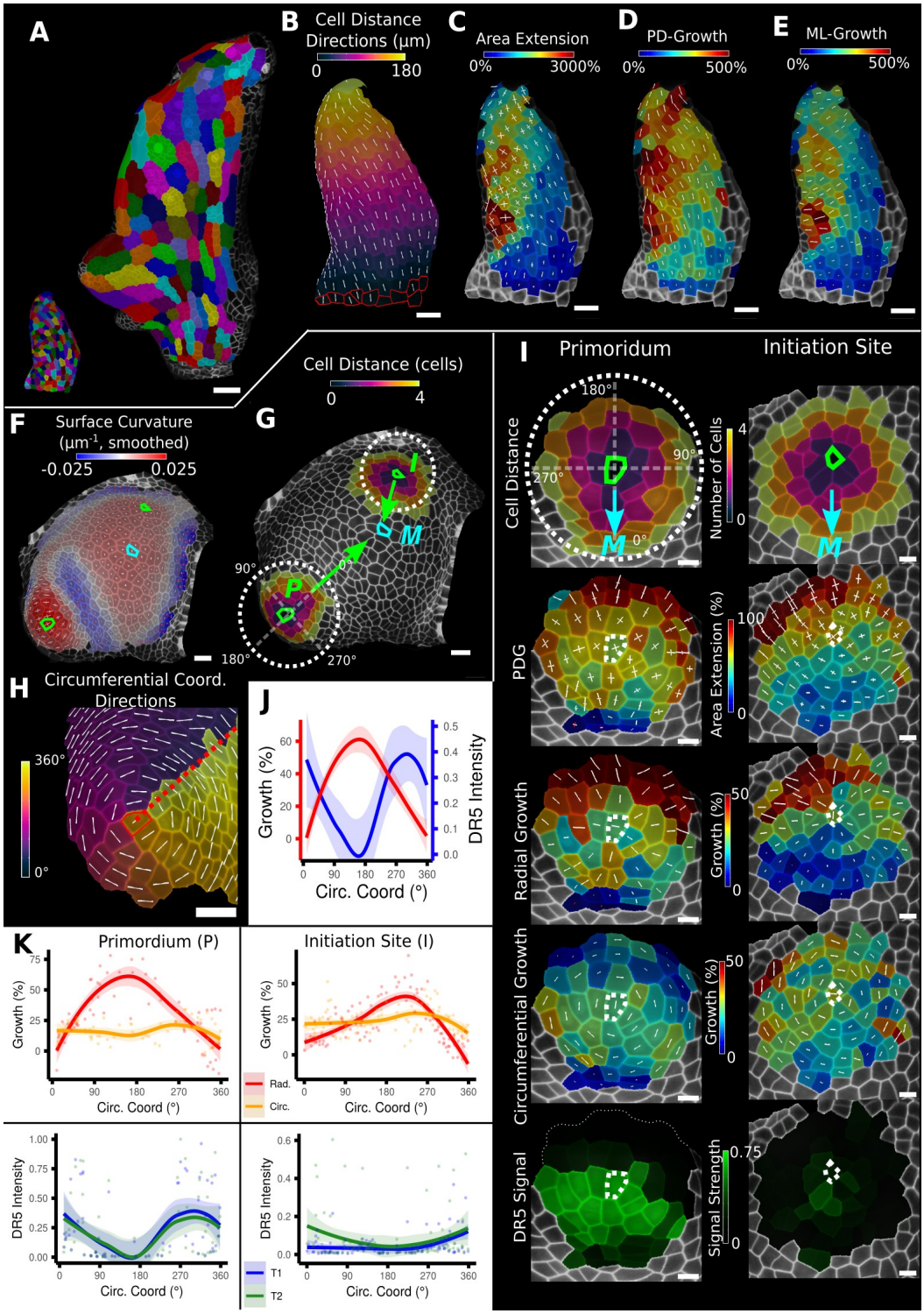

Figure 3: Examples of data analyses using organ coordinate directions. (A-E) Quantification of cellular growth along organ axes in a young *A. thaliana* leaf. (A) Segmented meshes of the leaf primordium at 3 and 6 days after initiation shown with cell labels and lineages of the earlier time

point (3 days). (B) Earlier time point of (A) with proximal-distal (PD) axis coordinates (heat map) and directions (white lines) computed from selected cells at the leaf base. (C) Area extension (heat map) and Principal Directions of Growth (PDGs, white lines) between the time points of (A). PDG axes are computed per cell and can point in different directions. (D-E) Computation of the growth component of (C) that is directed along the PD and the orthogonal medial-lateral (ML) axis. (F-K) Quantification of locally directed growth in leaf primordium and initiation site of a tomato meristem. (F) Smoothed heat map of cell curvature. Local maxima in this heat map (green & cyan cells) were selected as meristem center (M), primordium center (P) and initiation site (I) as shown in (G). (H) To analyze the data we defined a circumferential coordinate system with its axes directions (white lines) around the primordium and initiation center (not shown), and aligned them towards the meristem center. (I) Heat maps of cell distance, area extension, radial and circumferential growth and normalized DR5 signal intensity of the aligned primordium and initiation site. (J) Plotting the data of (I) reveals a negative correlation of the DR5 signal intensity and radial growth around the developing primordium. (K) Detailed plots of radial (red) and circumferential growth (orange) as well as the normalized DR5 signal intensity of the primordium and initiation site. Scale bars: (A) 50 µm; (B - H) 20 µm; (I) 10 µm. See also user guide sections 16 “Custom axis directions”, 23 “Organ-centric coordinate systems” and tutorial video S3 available at **https://doi.org/10.5061/dryad.m905qfv1r**.

Combining directions

In 2D or on 2.5D surfaces, local directions can be fully defined by a single distance measure, by taking one direction aligned with the gradient of the distance field or a Bezier curve, and the other perpendicular to the first. This is similar to methods used to specify directions in developmental modeling in plants (Green et al., 2010; Kennaway & Coen, 2019; Kierzkowski et al., 2019; Kuchen et al., 2012; Whitewoods et al., 2020), and thus facilitates direct comparison between models and experimentally observed patterns of growth and gene expression.

In 3D, a third direction must be defined (Kennaway & Coen, 2019; Whitewoods et al., 2020). In MorphoGraphX this can be done by combining the directions defined by different distance measures. The 3D Cell Atlas add-on (Montenegro-Johnson et al., 2015) combines several distance measures for radially symmetric structures such as root and hypocotyls. A Bezier curve is placed along the center in the longitudinal direction and combined with a surface mesh to obtain radial directions (Figure 4B). This also puts bounds on the radial direction (and also implicitly on the circumferential direction) which allows relative coordinates to be assigned to cells in addition to absolute values. The relative radial coordinate will follow the layer as the root narrows towards the tip. The relative distance between the central axis and the organ surface can then be used to annotate and classify 3D segmented

cells in organs with a layered cellular organization. Figure 4D shows classification of layers with relative coordinates on an *Arabidopsis* root (Montenegro-Johnson et al., 2015). Figure 4C shows layer classification using absolute distance from a surface mesh (Montenegro-Johnson et al., 2019), which can be used as a starting point for layer classification in any organ.

The mature ovule in *Arabidopsis* shows a more complicated structure than a root or sepal, with five layers of integument cells encapsulating the nucellus that contains the embryo sac (Schneitz et al., 1995; Vijayan et al., 2021; Fig 1S1; Fig 5). In this example, combining different directions allows the establishment of organ-centric coordinates in the outermost layer of cells in the ovule (the outer integuement). After segmentation and 3D mesh extraction in MorphoGraphX, directions normal to the surface (Fig 5A) were combined with those of a Bezier curve computed from a user-selected cell file (Fig 5B,C). Similar to the root data, relative coordinates facilitate the classification of cells into layers.

The Bezier curve defined the longitudinal direction whereas the surface directions obtained from the organ surface mesh were used to compute perpendicular width and depth axes and distances. Cell volume and geometry acquired from 3D segmentation and mesh extraction (Fig 1S1) were calculated along the various directions of the organ axes and analyzed (Fig 5D-G).

Moving along the proximal-distal axis from 0-260 µm, we found variations in cell volume with a clear minimum at around 100 µm and a steady increase towards proximal and distal end (Fig 5G). Measuring the length, width and depth of cells separately revealed the underlying cause for differences in cell volume between different proximal-distal regions of the outermost integuement layer. At the proximal end (at 0 µm) the cell shape is relatively isotropic with similar values in cell length, width and depth. Moving along the proximal-distal axis, cell anisotropy slowly increased, first mostly due the decreasing depth and width (until around 100 µm), later mainly due to the increased cell length (from about 150 µm). The increased cell length suggests a highly anisotropic growth along the longitudinal axis in this area. A potential proliferative region could be suspected in the region between 100-150 µm, where cell volume and length are the smallest. The quantification using the organ coordinates in this study allows spatial information to be linked to 3D cellular properties such as cell volumes and the associated shape anisotropies along different cell axes.

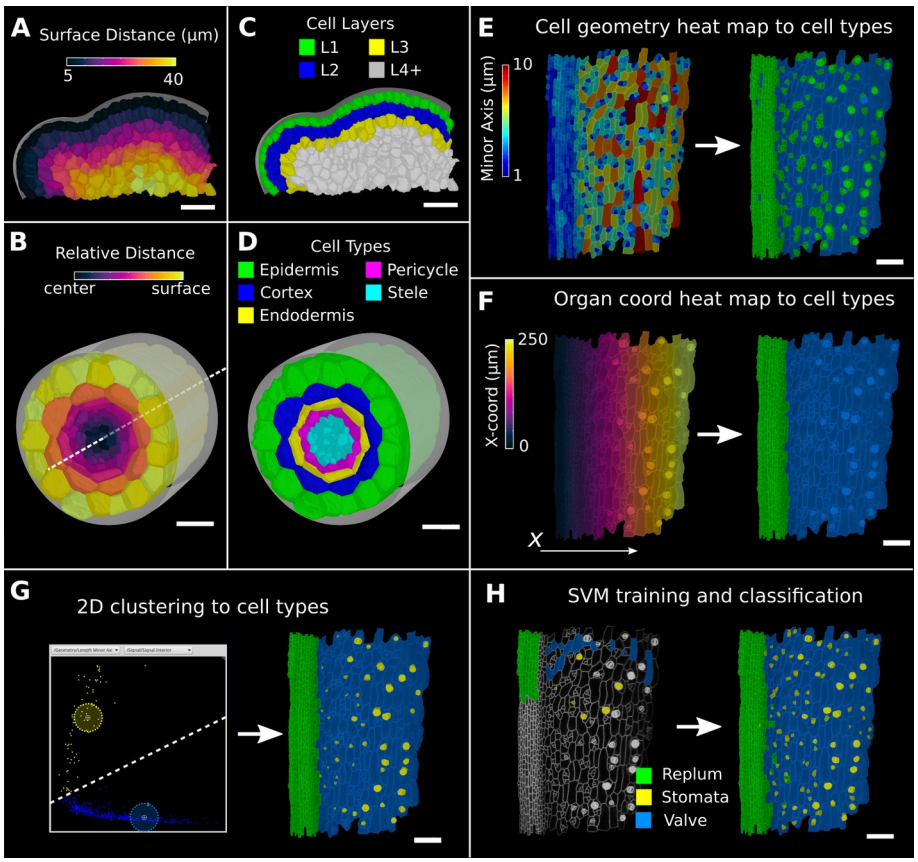

Figure 4: Methods to create organ coordinates for 3D meshes and to label different cell types. (A-D) Organ coordinates and cell types for volumetric meshes. (A) Heat map of the surface distance for cell centroids in an *A. thaliana* shoot apical meristem. (B) For volumetric tissues often a single direction is not enough to capture the geometry of the organ. Different methods can be combined such as a Bezier curve (white dashed line) with a surface mesh (grey) to create a heat map of the relative radial distance of cells in the *A. thaliana* root. (C-D) Organ coordinates can be used to assign cell type labels as demonstrated in the 3D Cell Atlas plugin for meristem and root. See also Figure 3-figure supplement 1. (E-H) Different methods to create cell type labellings. (E) *A. thaliana* gynoecium (fruit epidermis) surface segmentation with a heat map of the length of the minor cell axis as obtained from a PCA on the cells' triangles. The heat values can be thresholded to assign two cell types. (F) The same principle can be used on organ coordinates which results in a clean separation of replum (green) and valve tissue (blue). (G) We generalized the 2D clustering approach of 3D Cell Atlas (see Figure 3-figure supplement 1) so that it can be used for any measure pair and on subset selections of cells. Shown is a 2D plot of the minor axis length (x-coord) and cell signal intensity (y-coord) on the valve tissue in (F). Manually assigning clusters can separate the stomata, which are typically smaller with higher signal values (yellow) and the remaining valve cells (blue) efficiently. See also Figure 3-figure supplement 1 for 2D plots of all cells. (H) The Support Vector Machine (SVM) classification is able to separate the 3 shown cell types in a higher dimensional space by using a variety of different measures and a relatively small training set. Scale bars: (A-D) 20 µm; (E-H) 50 µm. See

also user guide section 24 “Cell atlas and cell type classification” and tutorial videos S3 and S4 available at https://doi.org/10.5061/dryad.m905qfv1r.

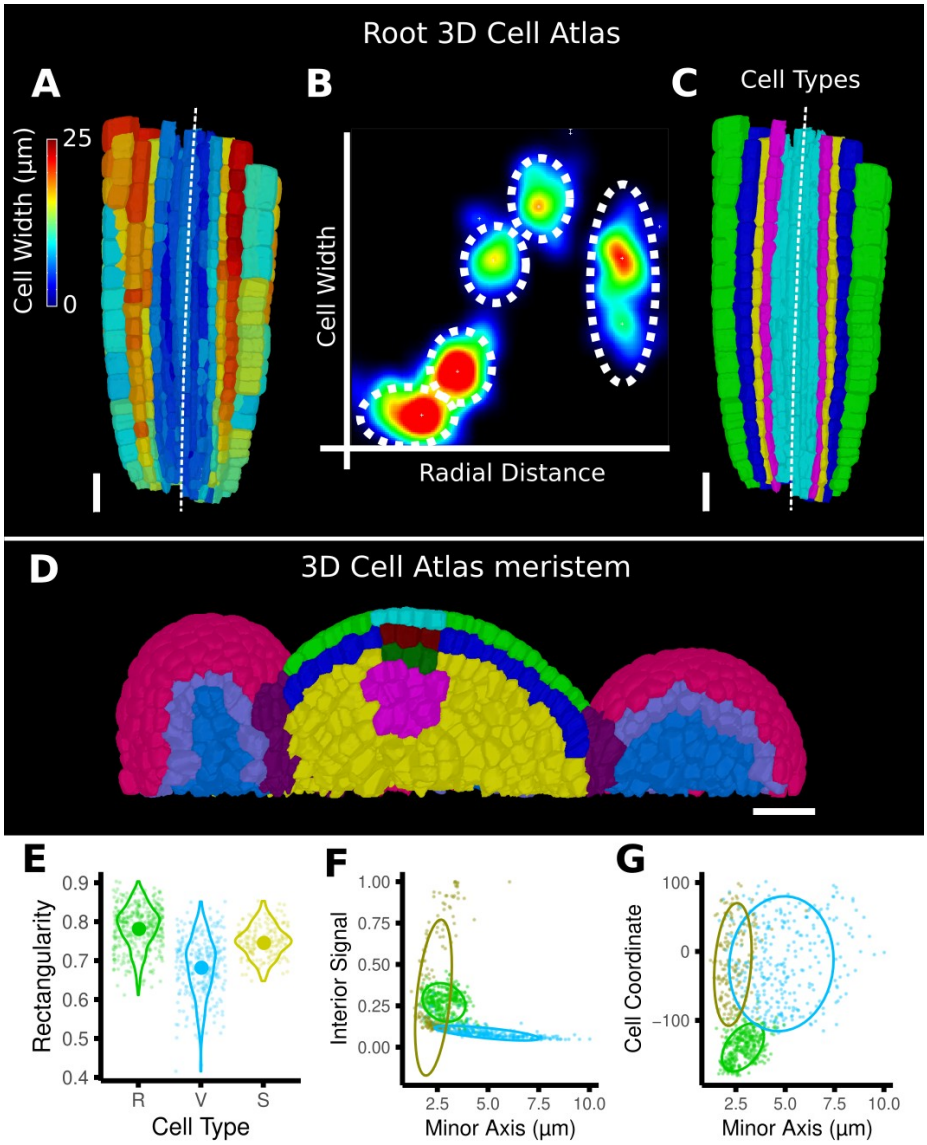

Figure 4-figure supplement 1: Cell type labeling methods and their use them in the data analysis. (A-C) Methods supported by the 3D Cell Atlas Add-on demonstrated on a *A. thaliana* root (Montenegro-Johnson et al., 2015). (A) Longitudinal cross section with a heat map of circumferential cell size. The white dashed line is the manually defined central axis. (B) The 2D heat plot of radial distance (heat map: in Fig 4B) and circumferential cell size (heat map in (A)) reveals a distinct clustering and can be used directly to assign the different cell types (dashed ellipses). (C) Final result of the cell type assignment. (D) The 3D cell atlas meristem (Montenegro-Johnson et al., 2019) allows the assignment of cell layers (as also seen in Figure 4C) and types in the meristem. (E-G) Cell type specific data analysis on the example of the *A. thaliana* gynoecium (Figure 4E-H). (E) Violin plot of the rectangularity of different cell types. Valve tissue cells are less rectangular and have higher variance compared to replum cells and stomata. (F-G) 2D scatter plots with fitting ellipses. Choosing different measures as x- or y-axis

allows the separation of different cell types as demonstrated in Figure 4G. Scale bars: (A, C, D) 20μm.

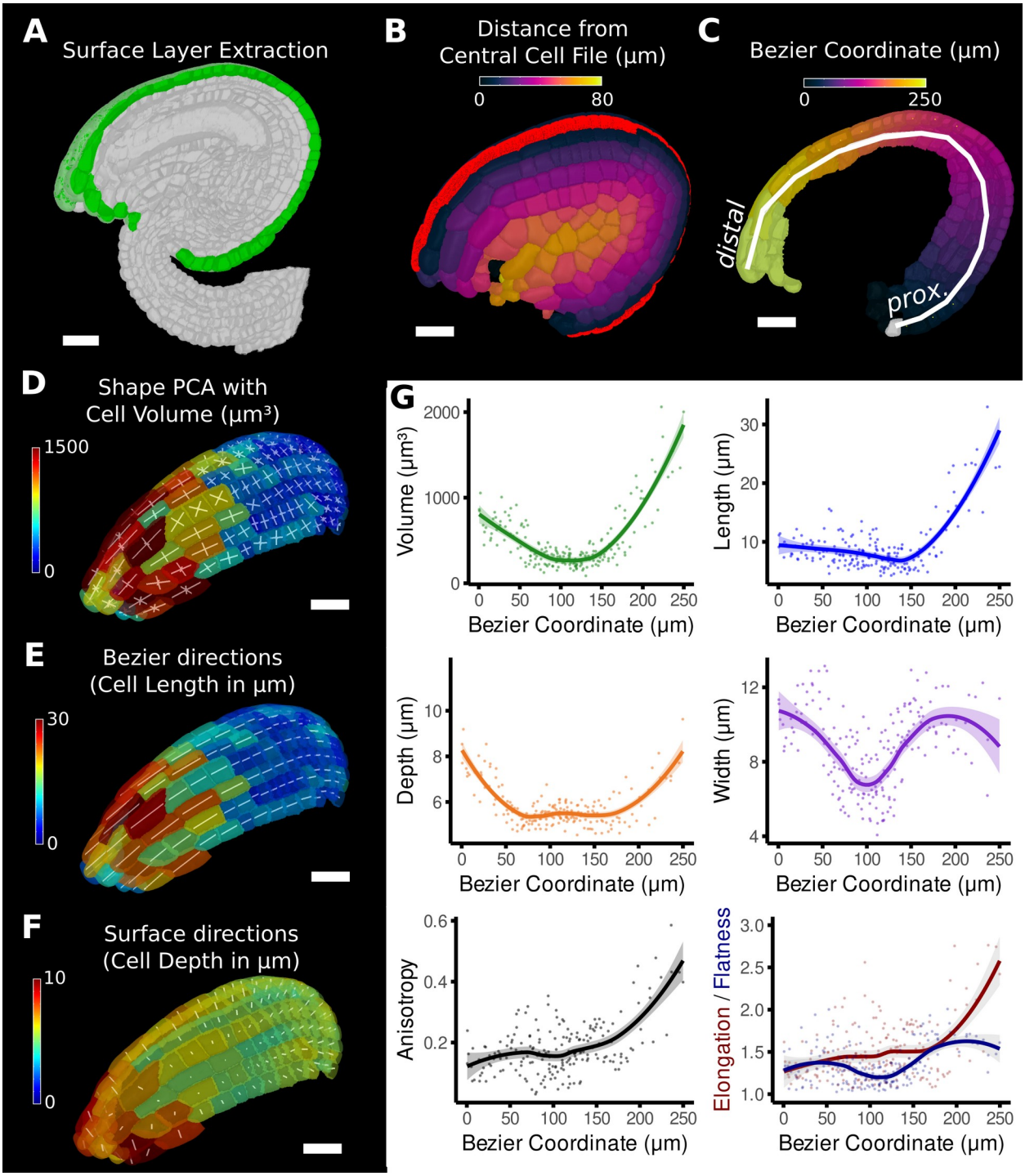

405 **Figure 5:** Quantification of volumetric cell sizes along organ axes in the outer layer of the outer integuement of an *A. thaliana* ovule. (A) Extraction of cell layer of interest (colored in green) using an organ surface mesh. (B) Selection of the central cell file (in red) with cell distance heat map to exclude lateral cells (heat values >40um). (C) The centroids of the selected cells from (B) were used to specify a Bezier curve defining the highly curved organ axis from the proximal to

the distal side. Heat coloring of the cells according to their coordinate along the Bezier. (D-F) Analysis of the cellular geometry in 3D. (D) Heat map of cell volume and the tensor of the three principal cell axes obtained from a Principal Component Analysis on the segmented stack. (E) Bezier directions and associated cell length. (F) Directions perpendicular to the surface and associated cell depth. (G) Plots of the various cellular parameters relative to the Bezier coordinate. A few small cells at the distal tip of the integuments were removed from the analysis. Scale bars: 20µm. See also user guide sections 21-24 and tutorial video S3 available at https://doi.org/10.5061/dryad.m905qfv1r.

Using positional information for automatic cell type classification

Plant organs typically emerge as primordia consisting of undifferentiated tissue. Cells subsequently differentiate, acquiring a unique identity that depends on their location within the organ, via genetic processes that integrate spatial and environmental cues. Although cell differentiation is ultimately controlled by differential gene expression, it is often the case that cell fate can be predicted by geometry, even at very early stages (Yoshida et al., 2014). It is rare that cells with different cell type have identical morphological features.

MorphoGraphX supports a large variety of measures to quantify different features of cell morphology, including simple geometric measures (area, volume, perimeter, surface area, min and max axis), shape quantifiers (convexity, circularity, lobeyness, largest empty circle, aspect ratio), neighborhood measures (number of neighbors, variability), gene expression (average, total, near boundary), and cell network measures (betweenness centrality, betweenness current flow). Most measures can be used on time-lapse data to quantify changes over time (growth rates, gene expression changes, cell proliferation). For a complete list of the measures implemented in MorphoGraphX, see Tables 1 and 2. The modular architecture of the software also allows custom measures tailored to specific problems to be easily added through its plug-in interface. More sophisticated calculations, for example the averaging of data over multiple samples, can be calculated externally in packages such as R and imported back into MorphoGraphX for visualization on segmented meshes. Here, the development of more complex data-flows is enabled by the use of a standardized attribute system to store and visualize cell data, for both scalar values and tensor (directional) information.

During the segmentation process MorphoGraphX assigns a unique label to each cell. When tracking cell lineages over multiple time points, a secondary label called the “parent label” is provided. Other secondary labelings are also possible, for example for cell type, cell layer, or zones within an organ. MorphoGraphX has several methods to assign these labels to classify cell types and layers. These labels can be assigned manually by interactively selecting cells, or by employing a number of processes that use heat map measure data to assign secondary labels (Fig 4E-H). Positional information from the distance measures can be combined with measures of cell morphology and gene expression, where a secondary labeling can be used to provide additional context.

Since cells of a common biological cell type have similarities in one or more geometrical, positional or gene expression attributes, the values of these attributes will often form a cluster, facilitating their automatic classification. An example can be seen in the 3D Cell Atlas addon for MorphoGraphX (Fig 4S1A-C; T. D. Montenegro-Johnson et al., 2015) that clusters cells by relative radial distance and cell size to classify the cell layers of the root, hypocotyl, mature embryo, or other radially symmetric plant organs. To aid in optimizing cell clustering, MorphoGraphX offers a two dimensional interactive heat map, where information from two independent measures can be visualized, and clusters selected (Fig 4S1B, 4G). These methods can be used repeatedly on sub-sets of cells to enable a classification of cells that differ across more than 2 features.

Multi-feature classifications tasks can be solved automatically by machine learning approaches (Cortes & Vapnik, 1995) when provided with sufficient training data. Of particular relevance are Support Vector Machines (SVMs) which have been used to classify cell types based on geometrical features of plant cells (de Reuille & Ragni, 2017; Sankar et al., 2014) . MorphoGraphX provides a simple interface to the libSVM support vector machines library (Chang & Lin, 2011). Cells can be selected and classified into different cell types for use as training data (Fig 4H, Video 2). Any cell attribute or measure that can be quantified in MorphoGraphX can be used by the classifier. These include all the morphological and gene expression measures, time-lapse measures, positional information created via distance maps or other coordinate systems, and even custom measures created via plugins or calculated externally with R or MATLAB. Once trained on a small group of cells with the desired measures, the classifier can be used to classify all the cells in a sample (Fig 4H). After manual curation, the classification can then be used as additional training data, improving the power of the classifier. Figure 4G,H and 4-figure supplement 1F-G shows the cell types of the *Arabidopsis* gynoecium which consists of the lateral valve tissues which are fused to the replum. Within the valve stomata are homogeneously distributed, consistent with the uniform growth and differentiation of this tissue. In contrast, no stomata cells can be found within the replum, which is made up of smaller, more homogenously sized cells. Cell typing this organ can be useful to identify the region of the valve margin, where the fully matured fruit will dehisce to release the seeds (Eldridge et al., 2016; Ripoll et al., 2019).

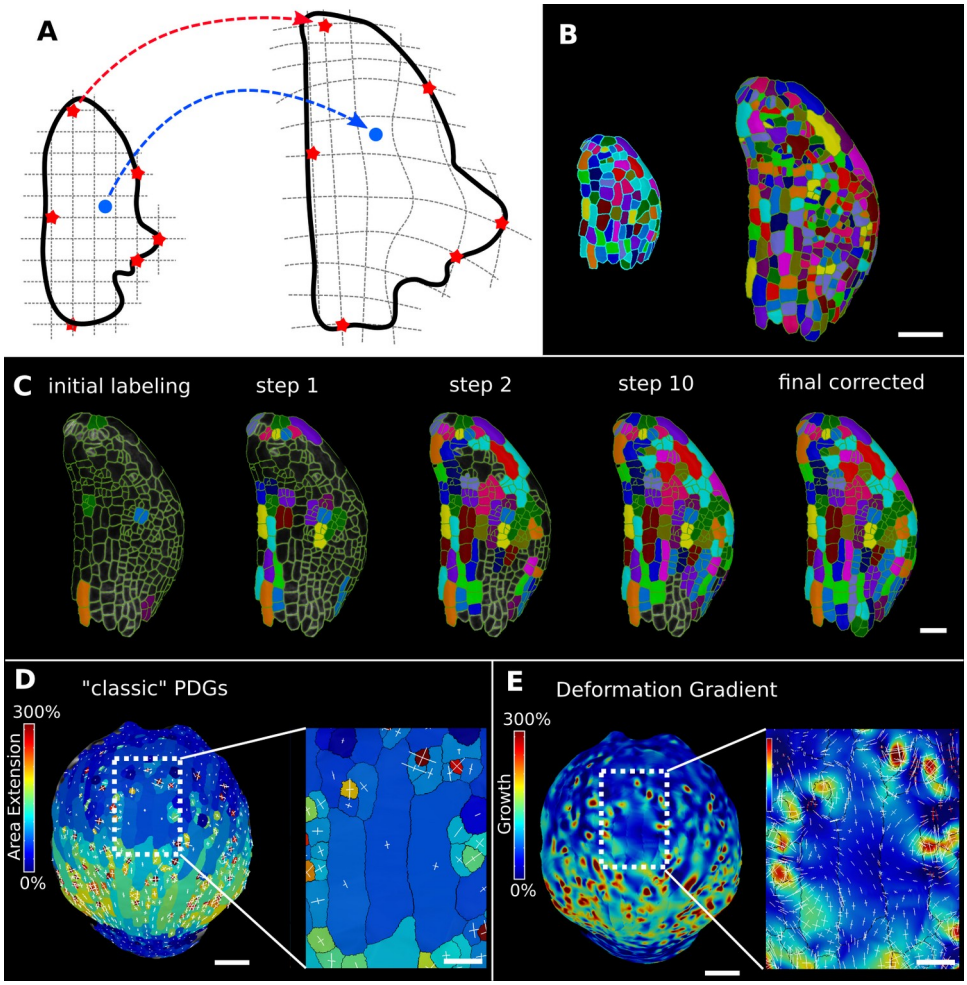

Figure 6: Deformation functions in MorphoGraphX. (A) Deformation functions allow a direct mapping of arbitrary points (blue) between two meshes. They require the definition of common landmarks (red stars). (B-C) Semi-automatic parent labelling using deformation functions. (B) Two consecutive time points of an *A. thaliana* leaf primordium segmented into cells. (C) The automatic parent labelling function requires the definition of a few manually labelled cells as initial landmarks. From this sparse correspondence, a mapping between the meshes can be created and new cell associations between the two meshes are added and checked for plausibility. With more cells found, the mapping between the meshes is improved for the next iteration. (D-E) Comparison of the classic Principal Directions of Growth (PDGs) in (D) with the gradient of a deformation function computed using the cell junctions from a complete cell lineage in (E) on an *A. thaliana* sepal. The classic PDGs compute a deformation for each cell individually and are shown with a heat map of areal extension for each cell. In contrast, the deformation function is a continuous function on the entire mesh. Here heat values are derived by multiplying the amount of max and min growth. Using the deformation function gradient reveals subcellular growth patterns that were previously hidden, such as differential growth within a single giant cell. Scale bars: (B, D, E) 50µm; (C & zoomed regions in D & E) 20µm.

See also user guide section 17 “Mesh Deformation and Growth Animation” and tutorial videos S1 and S2 available at https://doi.org/10.5061/dryad.m905qfv1r.

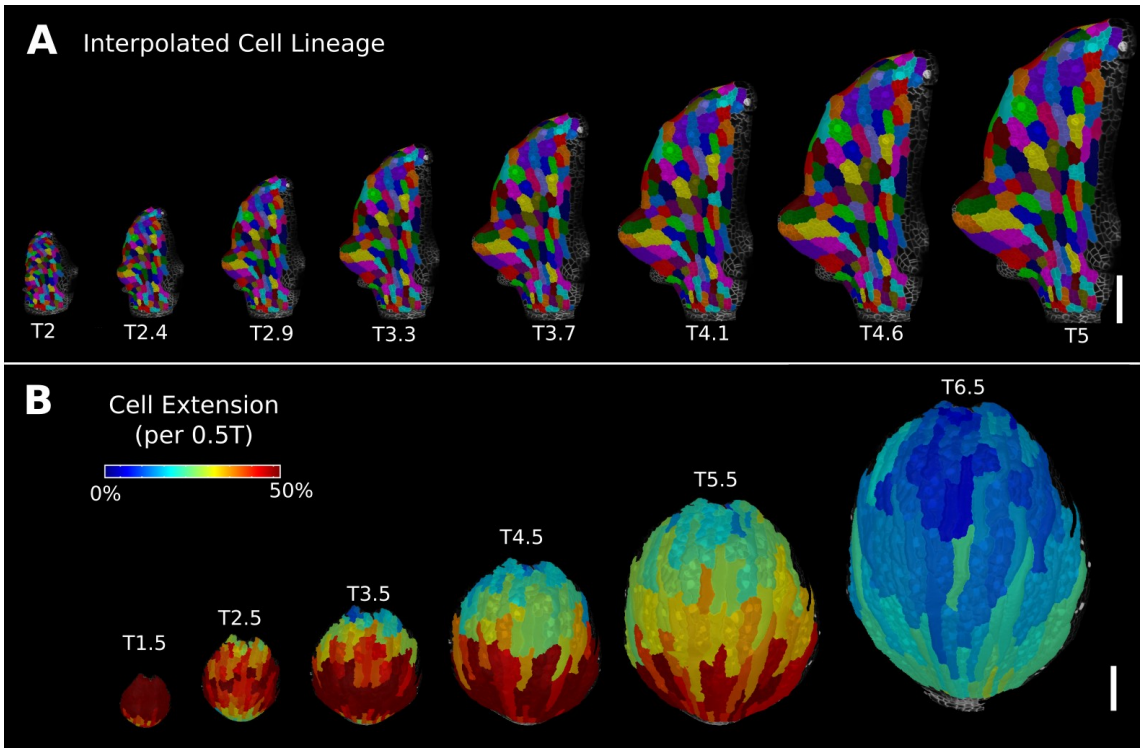

Figure 6-figure supplement 1: Deformation functions allow the interpolation of intermediate steps which can be turned into a continuous sequence or animation. (A) Animation of the early leaf development of *A. thaliana* created from T2 and T5 of Figure 5, shown with the lineages of T2. (B) Intermediate stages of the animation of the sepal growth of *A. thaliana*. For the actual timepoints see Figure 2-figure supplement 1. Scale bars: 100µm. See also user guide section 17 “Mesh Deformation and Growth Animation” and tutorial video S5 available at https://doi.org/10.5061/dryad.m905qfv1r.

Mapping positional information through time

In the analysis of morphogenesis, many key quantifications such as growth depend on the ability to track samples through time. In MorphoGraphX this can be done following cell segmentation by manually assigning parent labels to the second time point, a process that has been highly streamlined in the user interface for 2.5D surfaces. However for full 3D samples, or large 2.5D samples with multiple time points, this method can be cumbersome. One method to address this problem is to find a non-linear coordinate transformation or deformation that maps all the points from one time point onto the next. Parent labeling can then be determined by mapping cell centers of the later time point to an earlier one, allowing the cell they came from to be identified. This can be used to directly assign lineage, or to seed algorithms that use more involved methods, such as the minimization of the total distances between the mapped cells (Fernandez et al., 2010). In MorphoGraphX, to define a mapping between the meshes of two successive time points (Fig 6A) we have implemented a 3D deformation function based on scattered data point interpolation (using cubic radial-basis functions; Duchon, 1977; Turk & O'Brien, 1999). An initial transformation is computed based on a few preassigned landmarks, by matching several cells with their parents in the previous time point (Fig 6C). A deformation field is then calculated which provides a mapping for all points in 3D. This is then used to assign parent labels in the second time point based on their closest match in the previous time point. Close to the landmark points, this mapping will be very accurate, with accuracy decreasing with distance from the landmarks. The decrease in accuracy away from landmarks is larger if the deformation between the time points is highly non-uniform. After assigning all the cells their closest parent, the mapping is then verified by checking the correspondence of neighborhoods between each cell and its parent. The labeling for cells which do not match is cleared, and the process is repeated. This causes correctly labeled regions to "grow" out from the initially placed landmarks, until the entire sample is correctly labeled (Fig 6C; Video 3). At each step, only correctly labeled cells remain. Sometimes the iterative cell-labeling process can get stuck in highly proliferative areas where cells have divided repeatedly between time points. In this case a few additional landmarks can be manually added at trouble spots. One significant advantage of the method is that incorrect cells remain unlabeled, making manual curation straightforward. Once all of the parents are assigned and have passed the neighborhood correspondence check, one can be assured that both the lineage and the underlying segmentations are correct.

Deformation functions can also be used to create animations of organ development from 2.5D or 3D time-lapse data. This requires two or more time points of a segmented mesh with corresponding cell lineages. The cell centers and/or junctions are used as the landmarks defining the deformation function that maps one mesh onto the other. Interpolating mesh vertices between stages creates a smooth animation with as many intermediary steps as desired (Fig 6S1; Video 4). MorphoGraphX has a user-friendly pipeline to record animations directly from the GUI with options to adjust the camera angle and to visualize cell lineages, heat maps and cell outlines during the animation. Temporal smoothing of morphing animations created from more than two time points is achieved using Catmull-Rom splines to interpolate the position of mesh vertices over time (Catmull & Rom, 1974). Heat and signal values in the mesh, such as cell area, growth rates or gene expression can also be interpolated along with vertex positions.

In large cells, growth can vary significantly within the same cell (Armour et al., 2015; Elsner et al., 2018). As the deformation function provides a smooth mapping between time-points, its gradient can be used to create a continuous growth map at any point on a mesh. This enables the approximation of areal expansion and PDGs at a sub-cellular level, where the quality of the approximation is limited by the number and placement of landmarks (junctions). It is also possible to apply the process to subcellular landmarks, such as those obtained by tracking microbeads, as done previously for 2D images (Armour et al., 2015; Elsner et al., 2018). Our 3D implementation of this method has been used to compute growth directions on curved surface meshes (Fig 6E) and volumetric meshes (Fig 7I).

A comparison of the areal growth and PDGs calculated with deformation functions vs the cell-based method is shown in Figure 6D, E. The deformation function captures differences in growth within single cells, as is often apparent in larger cells that straddle areas of fast and slow growth. Figure 7A-I shows a 3D time-lapse of the *Arabidopsis* root where the deformation functions have been used to perform lineage tracking in 3D. It can be seen in Fig 7D that the 4 tissue types - epidermis, cortex, endodermis and pericyle - all show a similar pattern of cell volume increase, with slow growth in the meristem and faster growth near the transition zone, which can also be seen when displayed as a function of the distance from the root tip (Fig 7E). Most of the volume growth occurs along the longitudinal direction and is reflected by the increase in cell length, which is highly synchronized due to the physical connections of the cell layers (Fig 7F). Growth along width and depth directions are less synchronized, but much smaller than the

length increase, reflecting the strong anisotropic growth of this system (Fridman et al., 2021).

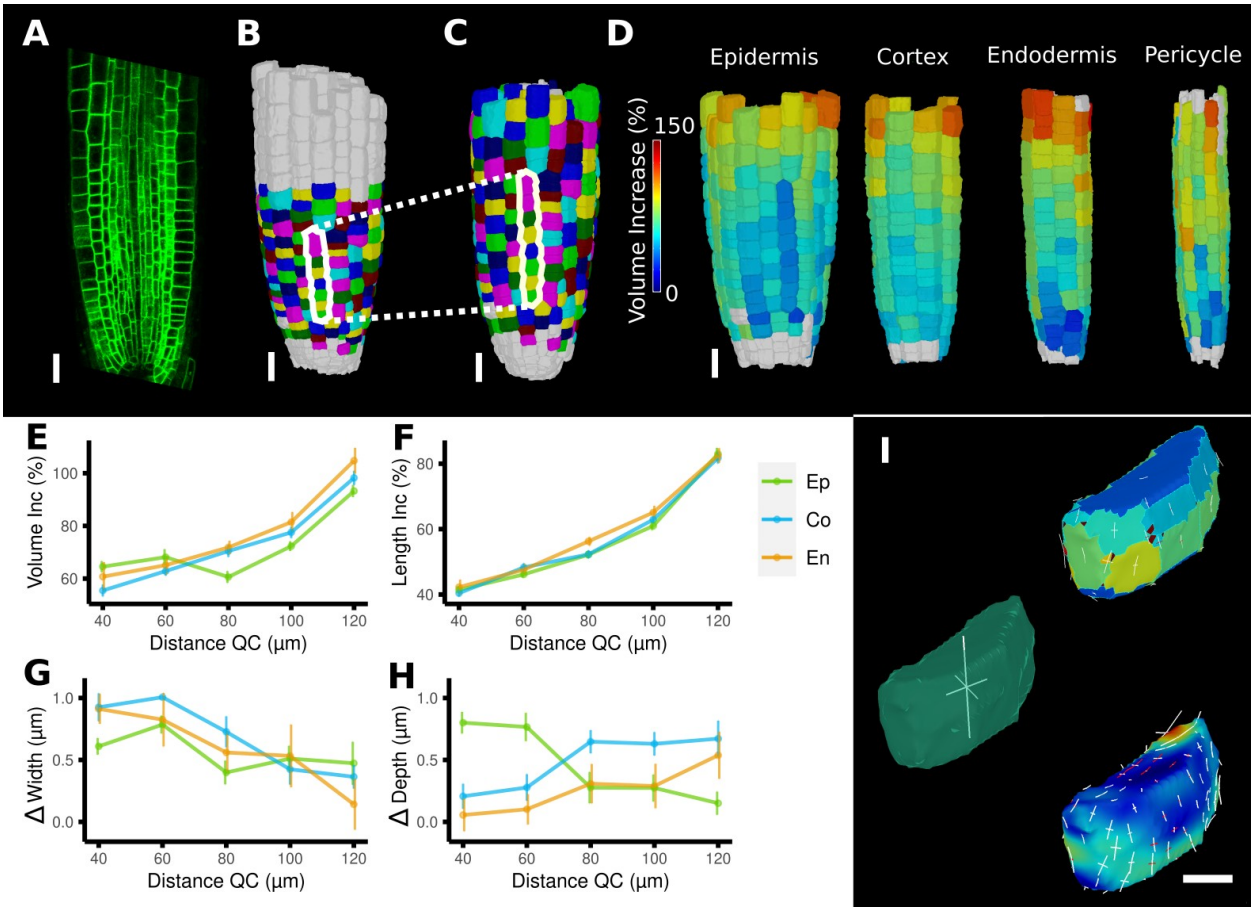

Figure 7: Time-lapse analysis and visualization of 3D meshes. (A) Cross section of the confocal stack of the first time point of a live imaged *A. thaliana* root. (B-C) The 3D segmentations of two time points imaged 6 hours apart. Shown are the cell lineages which were generated using the semi-automatic procedure following a manual correction. (D) Exploded view of the second timepoint with cells separated by cell types (see also Figure 4D). Cells are heat colored by their volume increase between the two time points. (E-H) Quantification of cellular growth along different directions within the organ. (E) Plot of the heat map data of (D). The cellular data was binned based on the distance of cells from the QC. Shown are mean values and standard deviations per bin. (F-H) Similarly binned data plots of the change in cell length (F), width (G) and depth (H). It can be seen that the majority of growth results from an increase in cell length. See Figure 7-figure supplement 1 for a detailed analysis of the cells in the endodermis. (I) Different ways to visualize 3D growth demonstrated using a single cortex cell: PDGs averaged over the cell volume (left), PDGs averaged over the cell walls projected onto the walls (top right), subcellular vertex level PDGs projected onto the cell walls (bottom right). Scale bars: (A-D) 20 µm; (I) 5 µm. See also user guide section 21 “Mesh 3D analysis and quantification” and tutorial video S6 and S7 available at https://doi.org/10.5061/dryad.m905qfv1r.

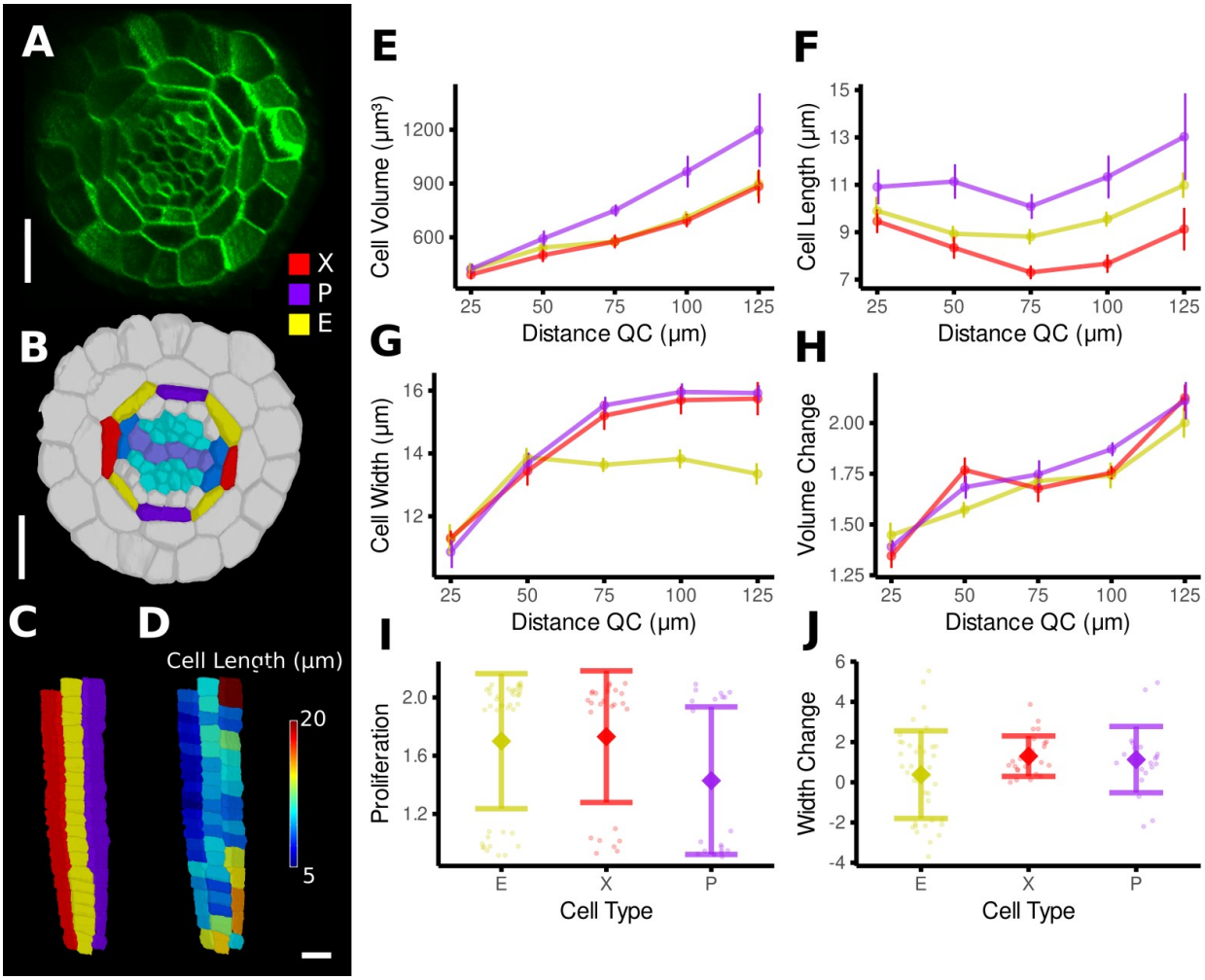

Figure 7-figure supplement 1: Time-lapse analysis of cellular geometry in the *A. thaliana* root endodermis. (A) Cross section of the confocal image of time point 1. (B) Segmentation with extended cell type labelling in the endodermis. The root cell type labelling of Fig. 3D was extended by identifying the xylem cells (light purple) in the stele (cyan), their adjacent pericycle cells (blue) and assigned the endodermis cells neighboring those pericycle cells as xylem file cells (X, red). Then the endodermis cells at right angles to the xylem files were assigned phloem file (P, purple) and the remaining other endodermis cells (E, yellow). (C) Side view of one cell file of each cell type. As the cell types do not change along the cell file, it was possible to automatically assign the cell files based on their circumferential coordinate. (D) Cell files of (G) with a heat map of cell length indicating smaller cells in the xylem pole. (E-J) Quantifications of cell geometry and development in the endodermis cell types. Cellular data was binned according to their distance from the quiescent center (QC) (E-H). Shown are mean values and standard deviations per bin (E-H) or cell type (I,J). Phloem file cells showed a larger volume (E), which was caused by a greater cell length (F), an observation which has been made before by (Andersen et al., 2018). In contrast, xylem file and other endodermis cells were smaller in

volume due to different reasons: While xylem file cells were the shortest (E), rest endodermis cells showed a lower cell width with increasing distance from the QC (G). The time-lapse analysis confirmed above observations: While volume change was similar across the cell type (I), phloem file cells showed a lower proliferation rate (H), whereas rest endodermis cells showed the smallest extension of cell width (J).Scale bars: (A, B) 20 µm; (C, D) 50 µm.

Advanced geometric analysis

In addition to tools for creating organ coordinates and deformation functions we have implemented a range of additional new processes in MorphoGraphX 2.0 for advanced image analysis.

3D lineage tracking and growth analysis. While MorphoGraphX was created to work with 2.5D surface projections, it now supports a complete set of tools for full 3D image processing, and in many samples advantages can be gained from combining both techniques. One example is automated cell lineage tracking, originally implemented for surfaces, that has now been extended to facilitate growth analysis in full 3D. Lineage tracking in 3D is a much harder task than on 2.5D surface images, as 3D cellular meshes lack the cellular junctions that serve as material points for surfaces. However in many cases entire organs are well defined by their surfaces meshes, allowing landmarks on the surface to be used to construct a 3D deformation function to aid lineage tracking in full 3D. Surface landmarks can also be combined with 3D cell centers and/or face centers as material points to improve the internal resolution of the deformation functions for full 3D samples. These techniques allow the methods used to calculate growth rates and PDGs in 2.5D to be extended to full 3D (Fig 7; Fridman et al., 2021). Cell proliferation and most of the other measures can also be quantified from 3D time-lapse data (Fig 7S1). In addition to the automated tools, improved manual 3D parent labeling and the ability to relabel cells so that adjacent cells are always a different color, aid in the manual curation of 3D lineage maps.

Cell division analysis. One of the more advanced quantifications from time-lapse data is the analysis of cell division. As plant cells cannot move, cell division and growth are the main determinants of morphogenesis. MorphoGraphX has processes to identify dividing cells from time-lapse data, and quantify the orientation of the division wall in both 2.5D and 3D (Fig 8A-I, Fig. 8S1). In 2.5D the best fit line to the division wall is calculated (Fig 8A,D), whereas in 3D the best fit plane is used (Fig 8B,C,G). There are also measures to determine the asymmetry of the daughter cells. The use of positional information to give organ context is especially important for directional information, such as the orientation of cell division. Quantifying the orientation of the division plane is of little use without knowing how it relates to the developmental axes. Orientations can be computed with respect to the axes of a local coordinate system defined for the organ, along with its associated positional information (Fig 8E,I, Fig 8S1A). It is also possible to quantify how close cell divisions are to common division rules

proposed in the literature, such as the shortest wall through the center of the cell including local minima (Fig 8H; Besson & Dumais, 2011, Yoshida et al. 2014, Valdepalli et al. 2021) along the principal directions of growth (Hejnowicz, 1984), or rules based on network measures (Jackson et al., 2019).

Cell connectivity networks. The organization of cells in organs may be analyzed through the extraction of cell connectivity networks from 2.5D or 3D segmented data. The physical associations between cells (cell-cell wall areas) can be extracted and converted into networks where they are analyzed using network measures (Fig 8J-K). Local measures such as the number of immediate neighbors (degree) can be calculated, along with more global measures, such as betweenness centrality based on the number of shortest paths cells lie upon, or random walk centrality (Fig 8K). These global measures are central to understanding how information flows within tissues (Jackson et al., 2017, 2019). The use of these measures uncovered the presence of a global property in cellular organization within the *Arabidopsis* SAM (Jackson et al., 2019). Namely, the length of paths between cells is maximized, whereby cells which lie upon more shortest paths have a great propensity to divide, and the orientation of this division tends to leave the two daughter cells on the fewest number of shortest paths. Using this approach, the local geometric properties of cells can be related to the emergent global organization of cellular arrangements. Perturbation of cell shape in the *katanin1* mutant led to alterations in path length in the SAM, which correlated with defects in phyllotaxis (Jackson et al., 2019).

Cell polarity. Cellular signals, such as proteins tagged with fluorescent reporters, can also be quantified in MorphoGraphX. After segmenting a surface into cells by using a cell wall stain or marker line, a signal collected in a second channel can be projected onto the surface mesh, and the abundance, orientation and polarity of signals can be computed. Examples are the PIN-FORMED (PIN) auxin transporter report line (Benková et al., 2003) or the GFP:MBD (Van Bruaene et al., 2004) line that tags microtubules (MTs), (Fig 8L-N, 8S2). For the quantification of cell polarity, MorphoGraphX implements a process where the projected signal along the cell border is binned based on its position in relation to the the cell center to obtain its predominant direction and its intensity. Figure 8L shows an example of the PIN1 polarity quantification at the cell wall of surface segmented cells in the SAM. A similar quantification can be performed for 3D meshes as shown in Figure 8N and Figure 8-figure supplement 2A,B where we computed the PIN2 polarity in epidermis and cortex cells of an *Arabidopsis* root. Again, this directional information can be combined with the organ coordinates to compute the angle

between cell polarity and the organ axis (Fig 8S2C). Another example is the quantification of MT alignment using our implementation of FibrilTool (Boudaoud et al., 2014) that has been adapted for processing on surfaces. After projecting the MT signal onto the surface, the alignment direction and strength of the signal can be quantified at the sub-cellular level (Fig 8M) or for entire cells (Fig 8S2E). Again, this information can be interpreted using organ coordinates, as we demonstrate on cells of a SAM which tend to have their MTs aligned circumferentially from the meristem center (Fig 8S2E).

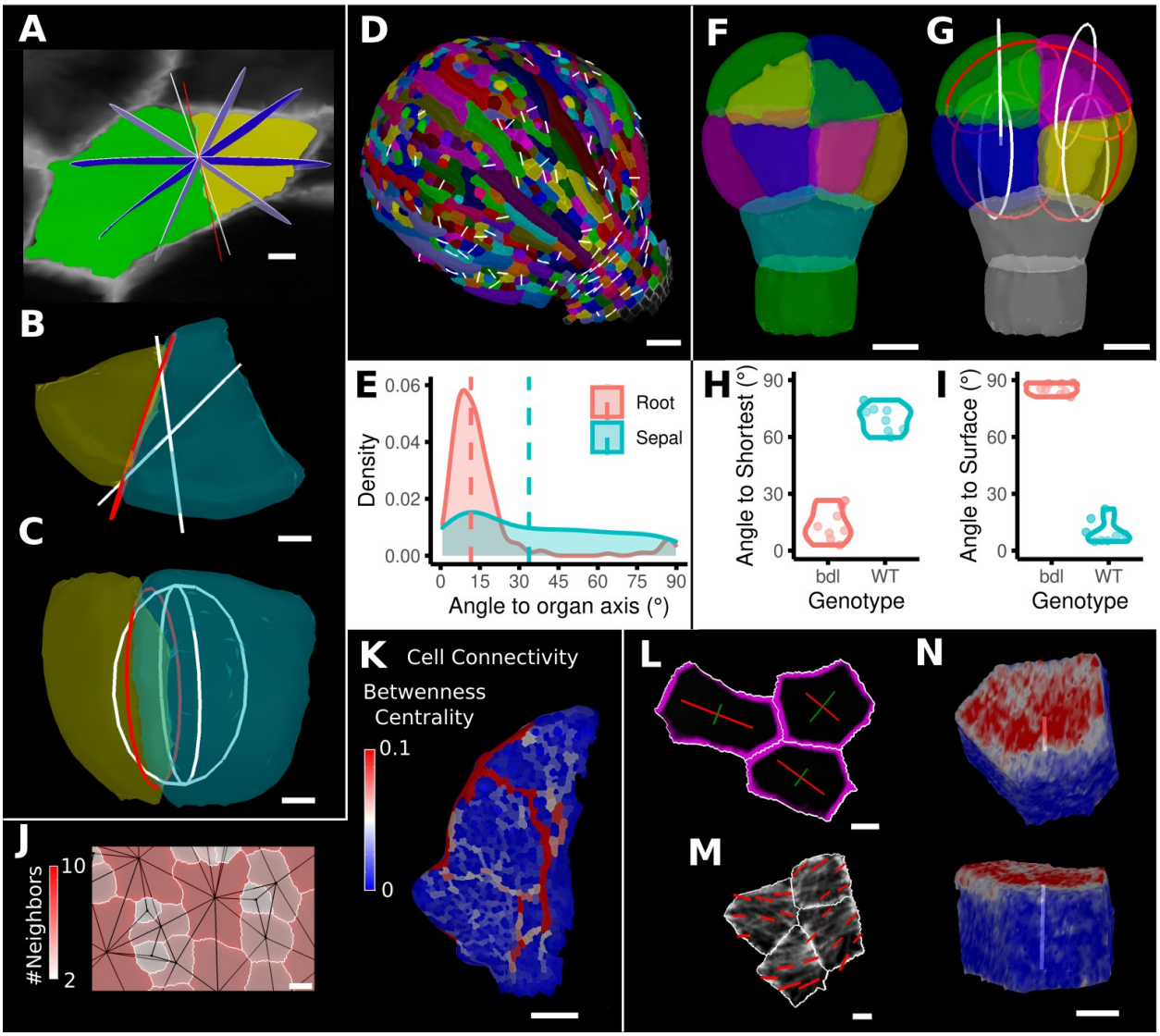

Figure 8: Advanced data analysis and visualization tools. (A) Division analysis of a cell from a surface segmentation of an *A. thaliana* sepal. A planar approximation of the actual plane is shown in red and other potential division planes in white/blue. The actual wall is very close to the globally shortest plane. (B-C) Top and side view of a recently divided 3D segmented cell. The daughter cells are colored yellow and cyan. The red circle depicts the flat approximation plane of the actual division wall. The two white rings depict the two smallest area division planes found by simulating divisions through the cell centroid of the mother cell (i.e. the combined daughter cells). (D) Visualization of the actual planes (white lines) between cells that divided into 2 daughter cells in the *A. thaliana* sepal. (E) Density distribution and median (dashed line) of the angle between the division plane and the primary organ axis in sepal (see D) and root (see Fig 8S1A). The division in sepals are less aligned with the organ axis. (F) Half of an *A. thaliana* wild type embryo in the 16 cell stage. This view shows that the divisions leading to this stage are precisely regulated to form 2 distinct layers in the embryo. (G) A visualization of the actual planes (red circles) and the shortest planes (white circles) in the wild type. Cells are colored

according to the label of the mother cells. (H-I) Violin plots of quantifications of the planes show that the wild type does not follow the shortest wall rule, unlike the auxin insensitive inducible bdl line RPS5A>>bdl. The bdl divisions are almost orthogonal to the organ surface (see Fig 8S1B, D, E), whereas the wild type divides parallel to the surface. Consequently, the bdl fails to form a distinct inner layer. (J-K) Cellular connectivity network analysis. (J) Cell connectivity network analysis on a young *A.thaliana* leaf. Cells are heat colored based on the number of neighbors. (K) Heat map of betweenness centrality. The betweenness reveals pathways which might be of importance for information flow, potentially via the transport of auxin. (L-N) Cell based signal analysis. (L) Analysis of cell polarization on a surface mesh. (M) Microtubule signal analysis on a surface mesh. (N) Top and side view of a cell polarization analysis on a volumetric mesh (root epidermis PIN2, see Figure 8-figure supplement 2A-D for details). Scale bars: (A,B,C,L,M) 2 µm; (D) 50 µm; (F,G,J,N) 5 µm; (K) 100 µm. See also user guide section 25 “Cell division analysis”.

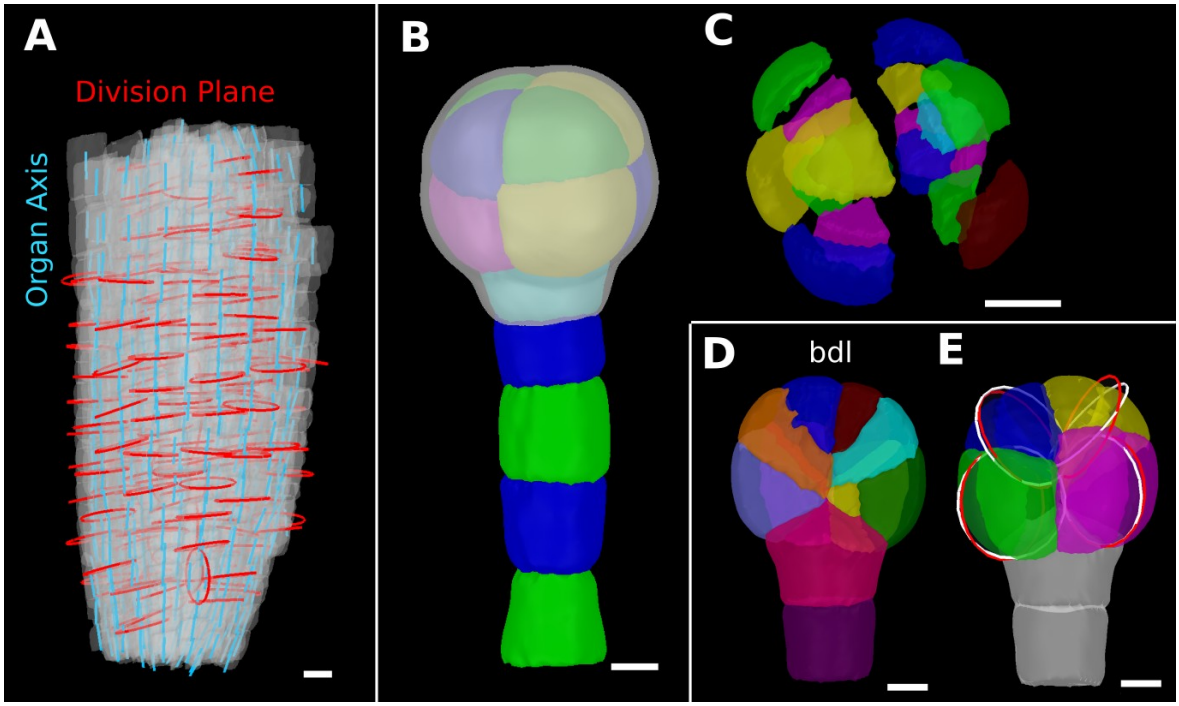

Figure 8-figure supplement 1: Details of the cell division analysis examples from Figure 8. (A) Second time point of an *A. thaliana* root (see Fig 7C) that was used for the division plane analysis in Figure 8E. Cells are shown semi-transparently (grey) with their longitudinal organ axis (cyan) obtained from the analysis using 3D Cell Atlas in Figure 4B. Planar approximations of the division planes between cells that divided between the 2 time points are shown as red circles. Consistent with the quantitative analysis in Figure 8E most planes are aligned with the organ axis. (B-C) Wild type embryo at the 16-cell stage segmented into volumetric cells shown with an organ surface mesh (grey, semi-transparent, B) and shown in an exploded view (C) to enable the visualization and access of inner layers. (D-E) Corresponding panels to Figure 8F-G for bdl embryo. Scale bars: (A,B,C) 10 µm; (D,E) 5 µm.

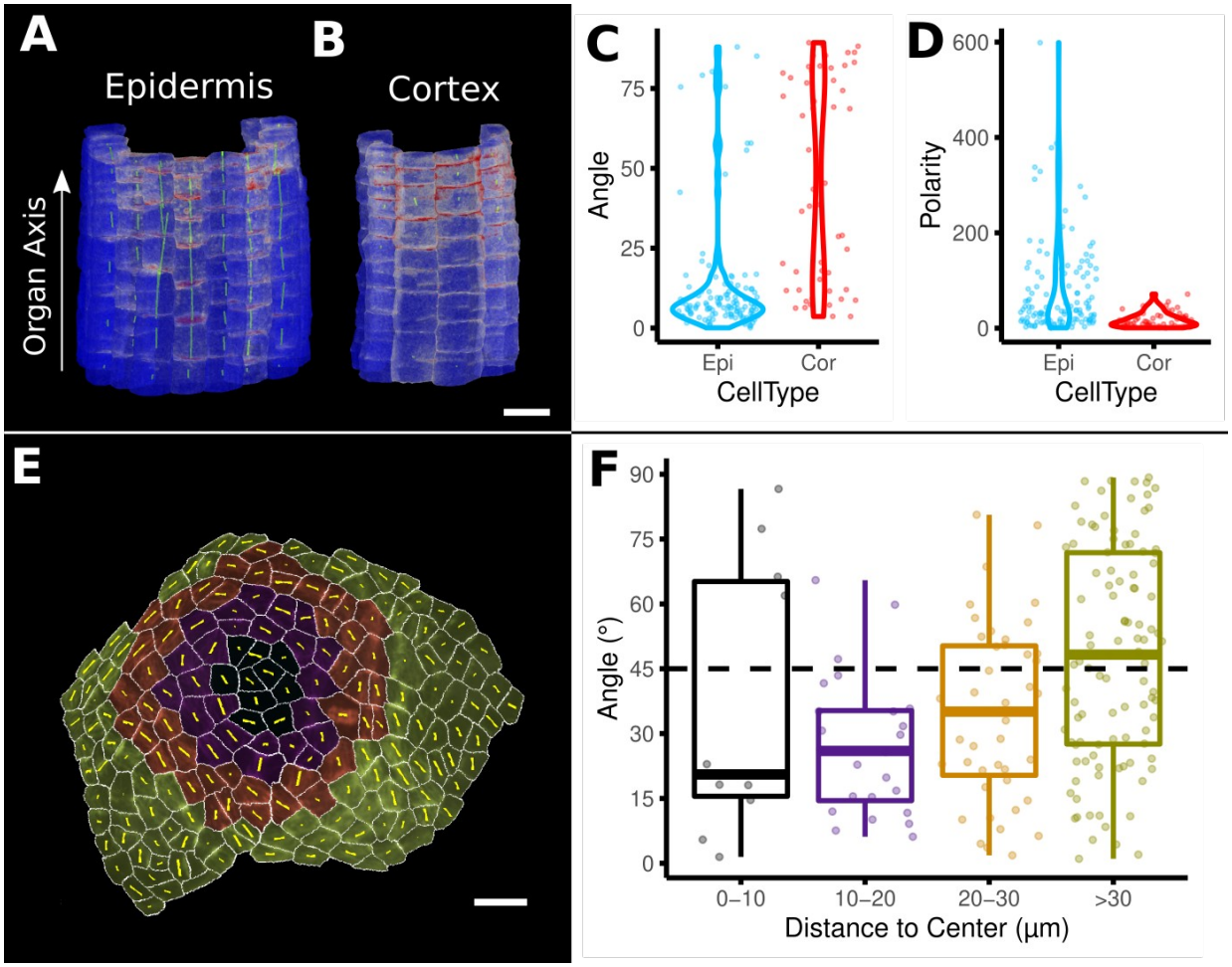

Figure 8-figure supplement 2: Example analyses of cell polarity and microtubule signals of the data shown in Fig 8M-N. (A-D) Quantification of PIN2 polarity in volumetric cells. (A-B) Heat map of PIN2 concentration on epidermis and cortex of an *A. thaliana* root. Green lines depict directionality and strength of the PIN2 concentration. (C-D) Violin plots of the orientation data for division planes and PIN2 polarity for epidermis and cortex cells. Epidermis cells show considerably stronger polarity (D) and are more aligned with the (longitudinal) organ axis (C). (E-F) Microtubule analysis on a Shoot Apical Meristem (SAM) of *A. thaliana*. (E) The cells on the SAM were binned according to their distance to the SAM center. Cells are heat colored according to their bin. Yellow lines show the direction and strength of the microtubule orientation. (F) Boxplot of the angular difference between microtubule orientation and the circumferential direction around the center of the SAM (similar to Fig 5H). Scale bars: (A,B) 20 µm; (E) 10 µm. See also user guide section 18 “Quantifying signal orientation”.

3D visualization and interactive tools

MorphoGraphX has a flexible rendering engine that can handle meshes containing millions of triangles. It supports the independent rotation and translation of different stacks and meshes in the same world space and the ability to render both voxel and geometric data together with blending and transparency. It has adjustable clipping plane pairs and a bendable Bezier cutting surface that can be used to look inside 3D samples, and an interface to support the creation of animations (Video 5). However, visualizing and interacting with 3D data on a 2D computer screen still remains a challenge. A particular problem is the validation and correction of 3D segmentations of organs, as internal cells are obscured by outer layers. 3D segmentation curation and correction is a bottleneck when developing training sets for deep learning tools, and MorphoGraphX has become a useful tool for this purpose (Wolny et al., 2020). In addition to clipping planes, exploded views are a commonly used method to visualize the internal structure of multi-component 3D objects (Li et al., 2008), which can be used on mesh data in MorphoGraphX. These are particular useful for visualizing the internal structure of entire organs with small cell numbers such as embryos (Fig 8S1C), and can be used in combination with multiple clipping planes for larger samples. To add biological meaning to the exploded visualization, cells can be bundled by their parent or cell type label to visualize key aspects of biological data sets such as cell divisions or to separate organs into cell layers or by cell type (Fig 7D, 8S1C). Furthermore, cells sharing the same cell type label can be easily manually selected, moved or deleted for improved visualization of specific tissues and groups of cells. These processes can also aid user interactions, making cell selection and annotation more straightforward when users are curating 3D cellular segmentations and lineage maps.

In addition to mesh editing tools, MorphoGraphX has several tools to edit voxel data. The simplest is an eraser tool which can be used to remove portions of the stack that would otherwise interfere with processing. An example is the digital deletion of the peripodial membrane overlying the Drosophila wing disc, which needs to be removed to allow for the extraction of the organ’s surface (Aegerter-Wilmsen et al., 2012). A typical workflow for 3D segmentation starts with a 3D image of a cell boundary marker. This is then pre-processed with operations such as blurring to reduce noise or background removal filters, before segmentation with algorithms such as the Insight Toolkit's (ITK) Morphological Watershed filter (www.itk.org). More recently, deep learning methods with convolutional neural networks (CNN) have been developed to predict cell boundaries, such as the 3D U-

Net model (Çiçek et al., 2016), that can improve the stacks for downstream segmentation. The modular structure of MorphoGraphX has allowed us to interface an implementation of the 3D U-Net model developed by Eschweiler et al. (2019). This enables the interactive use of the CNN boundary prediction tool from within MorphoGraphX (Video 6), and simplifies experimentation with different networks or downstream segmentation strategies. Several networks are currently implemented (Eschweiler et al., 2019, 2021; Wolny et al., 2020), although the add-on should work with any libtorch traced model. It also avoids the requirement to set up a full Python environment, and comes stand-alone as a package built for the most common nVidia GPU architechtures.

Once data is segmented, it often requires some manual correction before it is ready for final analysis in a chosen coordinate system. MorphoGraphX has interactive tools that operate on voxel data both to combine and split labels (cells), although typically it is easier to over-segment and combine, rather than under-segment and split (Video 6). This can be used to correct segmentations, which can then be used to help train deep learning networks to further improve automatic segmentation (Vijayan et al., 2021). In this context MorphoGraphX has been used to segment and curate *Arabidopsis* ovule data to create ground truth for confocal prediction networks (Wolny et al., 2020).

Software design

The internal architecture of MorphoGraphX has been designed to make it easily extendable, while retaining the speed of the fully compiled, statically typed language C++. The relatively small visualization and data management core is augmented with processes that are loaded dynamically at startup and provide almost all of the software's functionality. MorphoGraphX has grown to provide a wealth of custom processes for 2.5D and 3D image processing and coordinate system creation. Additionally, it has become a platform to integrate published tools and methods that have no visual interface to the data of their own, which increases their accessibility and ease of exploration for biologists. Examples include the previously mentioned deep learning tools, and the processes that interface to the Insight Toolkit (ITK) C++ image processing libraries. This greatly reduces the learning curve required to use ITK tools, such as the popular Morphological Watershed filter, which can be run from MorphoGraphX with a click of the mouse. For more advanced ITK pipelines, we have recently integrated an open source tool that provides an XML Pipeline Wrapper for the Insight Toolkit (XPIWIT) that

allows the development of ITK image processing pipelines interactively without any C++ programming required (Bartschat et al., 2016). These pipelines can be packaged into processes and called directly from the MorphoGraphX gui, allowing the easy exploration of complex ITK image processing pipelines. An example is the "Threshold of weighted intensity and seed-normal gradient dot product image" (TWANG) pipeline (Stegmaier et al., 2014), a fast parallel algorithm for nuclear segmentation. A selection of pipelines along with the XPIWIT software is bundled as an add-on for MorphoGraphX, and requires no additional installation.

Another example of software integration with popular open source tools is the processes we have developed to interface with R (Video 7) that provide plots for basic statistical analysis on attributes created in MorphoGraphX, including positional information provided by organ-centric coordinate systems. This simplifies the creation of the most commonly used plots without the need for export files and the mastery of ggplot. In addition to directly linking to C++ libraries, MorphoGraphX can be scripted with Python, allowing repetitive functions to be performed in batch, and the possibility to integrate Python-based tools. Operations interactively performed in MorphoGraphX are written to a Python log file for reproducibility and logging, and to allow easy cut-paste script creation.

Since its inception, a major focus of MorphoGraphX has been in the creation, manipulation and visualization of geometry in the form of surface meshes for 2.5D, and full 3D cellular meshes. This is in addition to the 3D voxel source data from microscopy images. There is currently very little software available that can handle both, and enable the interaction between the two. Most image processing software works only with voxels, whereas most computer graphics, animation and engineering software deals only with meshes. If the goal is simply to segment 2D or 3D cells, there are many options available, for example Fiji (Schindelin et al., 2012) or ilastik (S. Berg et al., 2019). If the processing of surface projections is required, advanced geometrical quantification like cell division analysis, or annotation with custom designed coordinate systems, then MorphoGraphX should be considered.

Conclusion

Similar to sequencing data, geometric data on the shape and sizes of hundreds or thousands of cells is of limited value without annotation. For many developmental

questions, the spatial context for information on cell shape, division and gene expression is paramount. However it is not enough to know the 3D position of cells, but rather their position in a coordinate system relative to the developing tissue or organism. These coordinates typically reflect the developmental axes of the organism or tissue, allowing the direct comparison of cell and organ shape changes with the gene expression controlling their morphology. In addition to putting data in a mechanistic context, organ-centric relative coordinates can be used to compare samples with different morphologies (Thompson, 1942), such as different mutants, or even in different species (Kierzkowski et al., 2019). This also applies to changes in morphology over time, where organ coordinate systems can be used to determine the correspondence between cells at different stages of development. Several tools have been published that successfully harness organ-centric coordinates for specific problems, for example in roots and hypocotyls (Montenegro-Johnson et al., 2015; Schmidt et al., 2014), the shoot apex (Montenegro-Johnson et al., 2019) and the *Arabidopsis* ovule and similar shaped organs (Vijayan et al., 2022). MorphoGraphX provides a generalized framework to create such tools by enabling the development of coordinate systems customized to the particular organ or organism of interest. Possibilities vary from simple distance-based systems to analyze leaf growth on surfaces from time-lapse images (Kierzkowski et al., 2019) to more involved methods for more complex organs in full 3D from fixed samples (Vijayan et al., 2021).

MorphoGraphX is unique in that it is the only software that we are aware of that allows image processing on surface meshes, which we informally refer to as 2.5D image processing. These meshes are most often created from 3D confocal images of a cell boundary signal. Images obtained from the microscope in proprietary formats are typically loaded into Fiji or ImageJ with BioFormats/LOCI-Tools (Linkert et al., 2010), and the converted to tiff for import into MorphoGraphX. Denoising of images and other pre-processing can be performed before import, however, most common pre-processing steps are now available directly in MorphoGraphX. Although originally targeted at 2.5D image processing, the necessity to handle full 3D image processing has meant that it has become convenient to implement a wide array of processing filters for full 3D in MorphoGraphX, many of which are GPU accelerated. The number of processes available in MorphoGraphX has swelled to over 540 in the current version, compared to just over 160 in the previously published version (Barbier de Reuille et al., 2015). This includes a comprehensive toolkit for cell shape analysis, growth tracking, cell division analysis, and the quantification of polarity markers, both on

2.5D image meshes, and for full 3D. All of these measures can be calculated and stored within the mesh, or exported to files for further processing with other software. Custom measures can also be calculated and imported for visualization within MorphoGraphX. Cell shape measures in combination with positional information provide a powerful framework for cell type classification, both with machine learning methods (Fig 4G-H) as well as clustering techniques (Montenegro-Johnson et al., 2019). Although organ-centric positional information provides important features for cell classification, it is unavailable in most machine learning cell classification software that typically can only deal with voxel information and limited annotation.

A key strength of MorphoGraphX is that it offers both manual and automatic tools for segmentation, lineage tracking and data analysis. Although fully automated methods are improving, streamlined methods for manual and semi-automatic segmentation and analysis provide a path to completion for many samples where the automatic methods are "almost" good enough. For example, the automatic lineage tracking now available in MorphoGraphX benefits from the streamlined tools we developed previously to do the process manually, as these are now used to correct and fill in missing portions when the automatic segmentation is incomplete. This reflects the interactive nature of MorphoGraphX and its focus on low-throughput but high-quality data sets.

As more and more imaging datasets are becoming available for community use, their annotation with positional information and gene expression data will be critical to help understand how the cell-level action of different genes and genetic networks is translated into the 3D forms of tissues and organs of different species (https://www.plantcellatlas.org). In this context MorphoGraphX provides a tool set to help maximize the attainable information from these datasets, in an accessible platform tailored to the experimental biologist.

Material and Methods

Software Availability

MorphoGraphX is open source software, and runs on Linux and Windows. Binaries and source code can be downloaded from:

www.MorphoGraphX.org/software

There are binaries available for recent versions of Ubuntu, as well as Windows. We recommend Linux as some add-ons are not available for Windows. For Linux we provide a Cuda version for machines with a compatible nVidia graphics card, and a non-Cuda version for those without. Currently there is only a non-Cuda version for Windows. Although there is no Mac version, some have had success running it in a virtual machine.

Support for the software can be found on the Help page of the MorphoGraphX web site, and the MorphoGraphX user forum on forum.image.sc.

With the growing number of processes in MorphoGraphX the complexity of the software has increased. We aim to provide novel users with sufficient documentation to do their first steps in MorphoGraphX. We previously published a detailed guide on how to generate cellular segmentations and do basic quantifications as shown in Figure 1 (Strauss et al., 2019). MorphoGraphX 2.0 also comes with an extended manual which contains step by step guides for all workflows presented in this paper (Table 3).

Data Availability

All new data collected for this manuscript, along with the specific version of MorphoGraphX used for analysis, and the tutorial videos are available online, and can be downloaded from Dryad here:

https://doi.org/10.5061/dryad.m905qfv1r.

Data Acquisition

Arabidopsis Flower Meristem (Fig 1)

pUBQ10::acyl:TDT (Segonzac et al., 2012) and DR5v2::n3eGFP (Liao et al., 2015) were crossed. F3 double homozygote line was used for imaging. Floral meristems were dissected from 2 weeks old plants grown on soil under the long-day condition (16 h light/ 8h dark), at 20°C ± 2°C using injection needle. Dissected samples were cultivated in 1/2 Murashige and Skoog medium with 1% sucrose supplemented with 0.1% plant protective medium under the long-day condition (16 h light/ 8h dark), at 20°C ± 2°C. Confocal imaging was performed with Zeiss LSM800 with a 40× long-distance water immersion objective (1 NA, Apochromat). Excitation was performed using a diode laser with 488 nm for GFP and 561 nm for TDT. Signal was collected at 500-550 and 600-660 nm, respectively. Images of 3 replicates were obtained every 24 hours for 4 days.

Arabidopsis Ovule (Fig 1S1, Fig 5A-F)

Data previously published in (Vijayan et al., 2021).

Arabidopsis Root (Fig 2A, Fig 4B,D, Fig 4S1A,C, Fig 7A-D,I, Fig 7S1A-D, Fig 8S1A)

Root imaging: pUBIQ10::H2B-RFP pUBQ10::YFP-PIP1;4 was described previously (von Wangenheim et al. 2016). The seeds were stratified for 1 day at 4°C, grown on 1/2 Murashige and Skoog medium with 1% sucrose under the long-day condition (16 h light/ 8h dark) at 20°C ± 2°C. Confocal imaging was performed with Zeiss LSM780 with two-photon laser (excitation 960nm) with a band pass filter 500/550nm for YFP. Images of 3 replicates were obtained.

Arabidopsis Mature Embryo (Fig 2C)

Arabidopsis thaliana Col-0 seeds were sterilized in 70% ethanol with Tween20 for two minutes, replaced with 95% ethanol for 1 minute and left until dry. Seeds were placed on the Petri plates containing 1/2 MS medium including vitamins (at pH 5.6) with 1.5% agar and stratified at 4°C for 3 days in darkness. Next, seeds were imbibed for 3 hours, and the mature seed embryo was isolated from the seed coat. For live imaging, the embryos were stained with propidium iodide 0.1% (Sigma-Aldrich) for 3 minutes and imaged with Leica SP8 laser scanning confocal

microscope with a water immersion objective (x20). Excitation wavelengths and emission windows were 535 nm and 617 nm. Confocal stacks were acquired at 1024x1024 resolution, with 0.5-µm distance in Z-dimension. Images were acquired at 48 hours intervals and samples were kept in a growth chamber under long-day condition (22°C, with 16 h of light per day) between imaging.

Marchantia Time-lapse (Video 3)

Marchantia polymorpha gemmaling Cam-1 PM::GFP reporter line (Shani et al., 2010) were transferred on a Petri plate containing 1/2 Gamborg's B5 medium including vitamins (pH 5.5) with 1.2% agar and grown for 24 hours. For live imaging, the gemmaling were imaged with Leica SP5 laser scanning confocal microscope with a water immersion objective (x25/0.95). Excitation wavelengths and emission windows were 488 nm and 510 nm. Confocal stacks were acquired at 1024x1024 resolution, with 0.5-µm distance in Z-dimension. Images were acquired at 24 hours intervals and samples were kept in a growth chamber under constant light between imaging. For the move we selected a representative sample from 6 total replicates. To quantify the cell area, change and anisotropy, the fluorescence signal was segmented and semi-automated parent labelling as performed to couple the cells at two successive time points. Heat-maps are displayed on the later time-point (after 24 hours of growth). Scale bars are displayed on the image.

Arabidopsis Sepal (Fig 2D,E, Fig 2S1A,B, Fig 6D,E, Fig 6S1B, Fig 8A,D)

Data previously published in (Hervieux et al., 2016).

Arabidopsis Leaf (Fig 3A-E, Fig 6S1A, Fig 8J,K)

Data previously published in (Kierzkowski et al., 2019).

Tomato Shoot Apical Meristem (Fig 3F-I)

Data previously published in (Kierzkowski et al., 2012).

Arabidopsis Shoot Apical Meristem (Fig 4A,C, Fig 4S1D)

Data previously published in (Montenegro-Johnson et al., 2019).

Arabidopsis Gynoecium (Fig 4E-H) and Leaf (Fig 6B,C)

pUBQ10::acyl:YFP has been described previously (Willis et al., 2016). Plants were cultivated on soil under the long-day condition (16 h light/ 8h dark), and 20°C ± 2°C. Flowers at post-anthesis stage from 5 weeks-old plants were dissected with fine tweezers to remove sepals and stamens to expose gynoecium and mounted on the 60 mm plastic dish filled with 1.5% agar. Confocal imaging was performed with a Zeiss LSM800 upright confocal microscope, equipped with a long working-distance water immersion objective 40X (1 NA, Apochromat). Excitation was performed using a diode laser with 488 nm for YFP and the signal was collected between 500 and 600 nm. For both organs images of 3 replicates each were obtained.

Arabidopsis Embryo (Fig 8B,C,F,G, Fig 8S1B-E)

Data previously published in (Yoshida et al., 2014).

Arabidopsis Shoot Apical Meristems for PIN1 and MT (Fig 8L,M, Fig 8S2A-C)

pUBQ10::acyl:TDT (Segonzac et al., 2012) and GFP:MBD (Van Bruaene et al., 2004) were crossed. F3 double homozygote line was used for imaging.

Floral organs were removed with fine tweezers about 21 days after germination to expose inflorescence meristem. Meristems were mounted on the 60 mm plastic dish filled with 1.5% agar and imaged with a Zeiss LSM800 upright confocal microscope, equipped with a long working-distance water immersion objective 60X (1 NA, Apochromat). Excitation was performed using a diode laser with 488 nm for GFP and 561 nm for TDT. Signal was collected at 500-550 and 600-660 nm, respectively. Images of 3 replicates were obtained.

Arabidopsis Root for PIN2 in 3D (Fig 8N-O, Fig8S2 E)

pPIN2::PIN2:GFP was previously described (Xu & Scheres, 2005). The seeds were stratified for 2 days at 4°C, grown on 1/2 Murashige and Skoog medium with 1% sucrose under the long-day condition (16 h light/ 8h dark) at 20C° ± 2°C. The roots were stained by 10µM propidium iodide (Sigma-Aldrich), and observed by Zeiss LSM780 with two-photon laser (excitation 990nm) with a band pass filter 500/550nm for GFP and 575-600nm for PI. Images of 3 replicates were obtained.

Data Analysis

For the data analysis examples in the paper we computed all necessary cellular data within MorphoGraphX and exported them as csv files (see MorphoGraphX user guide chapter 12 “Attribute maps & data export”). Those files were imported to RStudio for further processing or directly plotted using ggplot2 (R Core Team, 2020; RStudio Team, 2020; Wickham, 2016).

In the following, we provide a detailed description of the necessary processing steps for each data set shown in the figures. Hereby we refer to the relevant chapters in the extensive MorphoGraphX user guide for a step by step guide for more information.

Arabidopsis Flower Meristem (Fig 1)

We selected one sample for segmentation and further analysis. The segmentation, cell lineages and heat maps were generated following the standard workflow as described in (Strauss et al., 2019) and in the MorphoGraphX user guide (chapters 5 to 11).

Arabidopsis Ovule (Fig 1S1, 5)

We selected one sample of the published data for segmentation and further analysis (Vijayan et al., 2021). Segmentation was obtained by back blending the raw images to CNN boundary predictions (Wolny et al., 2020) as described in (Vijayan et al., 2021).

Following the segmentation (see also user guide chapter 20 “3D segmentation”), for Fig 1S1 we simply generated the heat map of the cell volumes (see user guide chapter 21.1 “Heat maps & Measures 3D”).

For the additional analysis in Fig. 5, we first generated a trimmed surface mesh (using the process “Mesh/Creation/Marching Cubes Surface” on the segmented stack) and then used it to label the outermost layer using the process “Mesh/Cell Atlas 3D/Ovule/Detect Cell Layers” which is based on the method described in (Montenegro-Johnson et al., 2019). Next we selected the cells of the cell type (or parent) label of the outermost layer, inverted the selection and deleted this selection. At this stage only the cells of the outer layer remained.

For each cell, its longitudinal organ axis (as custom cell axis X) was defined by a Bezier curve obtained from a manually selected central cell file using the processes “Misc/Bezier/Bezier From Cell File” and “Mesh/Cell Axis 3D/Custom/Create Bezier Line Directions” (see user guide chapter 16.1 “Custom Directions with Bezier” for general information about how to handle the Bezier in MorphoGraphX and chapter 21.6 “Custom Directions for 3D meshes” for its application for organ coordinates). Next, the surface organ axis (as custom cell axis Y) was computed using the surface mesh and the process “Mesh/Cell Axis 3D/Custom/Create Surface Direction”. Finally, the width direction (as custom cell axis Z) was computed as orthogonal direction of the other two using the process “Mesh/Cell Axis 3D/Custom/Create Orthogonal Direction”.

Next, the cell sizes were quantified by first doing a PCA on the voxels of cells in the segmented stack (“Mesh/Cell Axis 3D/Shape Analysis/Compute Shape Analysis 3D”, see also user guide chapter 22.2 “Cell shape analysis using Principal Component Analysis for 3D meshes”) and finally computing the component of the PCA’s tensor aligned with the axes of interest (“Mesh/Cell Axis 3D/Shape Analysis/Display Shape Axis 3D” with the appropriate “Custom” heat option), with the Bezier direction corresponding to cell length, the surface direction to depth and the orthogonal direction to width.

Shape Anisotropy was defined using the equation: (max - 0.5*min - 0.5*min)/(max+mid+min), with max, mid and min defined by the length of the PCA axes. Elongation is defined by max/mid and Flatness by mid/min.

To create the plots, cells with a distance >40µm from the central cell file were filtered out. The data of the remaining 213 cells was plotted.

Arabidopsis Root (Fig 2A, 4B,D, 4S1A,C, 7A-D,I, 7S1A-D, 8S1A)

From the 3 imaged replicates we selected the sample with the best segmentation quality for further analysis. The raw images of the two time points of the analyzed root data sample were blurred and segmented using the ITK watershed segmentation processes in MorphoGraphX (see also (Stamm et al., 2017) and the MorphoGraphX user guide chapter 20 “3D Segmentation”). From the segmented stack a surface mesh and volumetric cell mesh were created using the processes “Mesh/Creation/Marching Cubes 3D” and “Mesh/Creation/Marching Cubes Surface”.

For the axis alignment analysis in Fig. 2A, the organ was manually aligned with the y-axis and the coordinates of the cell centroids were computed (processes “Mesh/Heat Map/Analysis/Cell Analysis 3D” and “Mesh/Heat Map/Measures 3D/Location/Cell Coordinate” for the heat map; see also user guide chapter 21.1 “Heat maps and measures 3D” and 22.3 “Further types of organ coordinates”). In Fig. 2B the cell volume of the 304 epidermis cells was plotted against the y-coordinate.

The 3D Cell Atlas pipeline (Montenegro-Johnson et al., 2015; Stamm et al., 2017) was used to compute cell coordinates, sizes and cell types (Fig4B, D; Fig4S1A-C).

For the time-lapse analysis (Fig. 7A-I, Fig 7S1) the cell lineages were determined semi-automatically using the pipeline introduced in this paper (Fig. 6) followed by a manual error correction (see also user guide chapter 21.2 “Cell Lineage Tracking 3D”). Change maps were computed from the cells’ volume and size data extracted from 3D Cell Atlas from both time points (see user guide chapter 21.3 “Change Maps 3D”, chapter 24.1 “Cell Atlas Root” and (Stamm et al., 2017)). PDGs in 3D were derived from the deformation function mapping the first onto the second time point using parent labeled cell centroids and cell wall centers (see user guide chapter 21.4 “PDGs 3D”).

For the analysis of the cell types in the endodermis (Fig 7S1), xylem cells in the stele and their neighboring pericycle cells were automatically identified by their circumferential coordinate obtained from the previously executed 3D Cell Atlas pipeline (see above). Endodermis cells touching two xylem-associated pericycle cells were determined as xylem pole. The two phloem poles in the endodermis

were shifted by 90 degrees (or 2 cells) from the xylem pole. In total, we used 26 xylem pole, 21 phloem pole and 43 rest endodermis cells for the analysis.

For the analysis in Figures 8E and 8-figure supplement 1A only the second time point and its previously created parent labeling was used (see above). We computed the proliferation to the previous time point ("Mesh/Heat Map/Lineage Tracking/Heat Map Proliferation"), extracted the vertices on each division plane between cells that have divided exactly once (proliferation = 2, n=249 mother cells that divided) and computed a PCA on each set of division plane vertices to extract the normals of the planes (using the process "Mesh/Division Analysis/Analysis 3D/Division Analysis Multi", see also user guide chapter 25.2 "Division Analysis 3D"). Then we computed the angle between the longitudinal axis of the organ as extracted by 3D Cell Atlas and the division planes ("Mesh/Division Analysis/Compute Division Plane Angles") and exported the data.

Arabidopsis Mature Embryo (Fig 2C)

From more than 10 replicates a sample with curved overall shape was selected for the demonstration of the organ coordinates using a Bezier curve. The fluorescence signal was segmented on the surface, and cells were parent labeled manually between two successive time points following the standard pipeline (see (Strauss et al., 2019)) and the MorphoGraphX user guide (chapters 5 to 11)). For creating the heat map of organ coordinates, a Bezier line was created and manually aligned with the organ (see user guide chapter 23.2 "Bezier Line and Grid"). The organ coordinate heat map was then created using the process "Mesh/Heat Map/Measures/Location/Bezier Line Coord". The heatmap is displayed on the later time-point (after 48 hours of growth). Scale bars are displayed on the image.

Arabidopsis Sepal (Fig 2D,E, 2S1A,B, 6 D,E, 6S1B, 8A,D)

For the sepal analysis one replicate of the data from (Hervieux et al., 2016) consisting of 7 time points was used (see Fig. 2S1A,B).

For the analysis in Fig. 2D-F and Fig. 2S1 for each time point we manually determined the organ base based on the cell lineages from the first time point. Cells at the organ base were selected and used to compute the Euclidean cell distance measure ("Mesh/Heat Map/Measures/Location/Cell Distance", see also the user

guide chapter 23.1 “The cell distance measure”). Finally, cell distances, growth, proliferation and cell sizes were exported.

For the cell division analysis in Fig. 8A,B we analyzed the divisions that occurred between the time point T4 and T5 (n=84). We computed the proliferation between these time points, extracted the vertices on each division plane between cells that have divided exactly once (proliferation = 2) and computed a PCA on each set of division plane vertices to extract the normals of the planes (using the process “Mesh/Division Analysis/Analysis 2D/Division Analysis Multi”, see user guide chapter 25.1 “Division Analysis 2.5D”). Next, we computed the PD-axis direction of the organ using the Euclidean cell distance from the base using the previously computed cell distance measure (see above) for creating custom directions along the PD-axis (see user guide chapter 16.2 “Custom direction using a distance heat map”). Finally we computed the angle between PD-axis and the division planes (“Mesh/Division Analysis/Compute Division Plane Angles”) and exported the data.

For the growth analysis in Fig. 6D we computed the PDGs from time point T4 to time point T5, visualized on the earlier time point (see user guide chapter 15 “Principal Directions of Growth (PDGs)”). Fig. 6E shows the same time point, but here growth was computed using the gradient of the deformation function obtained from the cells’ junctions (see user guide chapter 17.6 “Growth analysis using deformation functions”).

Arabidopsis Shoot Apical Meristem (Fig 4A,C, 4S1D)

We selected one sample of the published data for analysis. Cell type labels were determined using the methods described in 3D Cell Atlas Meristem (Montenegro-Johnson et al., 2019). See also the user guide chapter 24.2 “Cell Atlas Meristem”. We computed the surface distance heatmap using a surface mesh and the process “Mesh/Heat Map/Measures 3D/Location/Mesh Distance” (see also user guide chapter 23.3 “Further types of organ coordinates”).

Arabidopsis Leaf (Fig 3A-E, 6S1A, 8J-K)

The *Arabidopsis* leaf data was previously published in (Kierzkowski et al., 2019). One replicate of a time-lapse series consisting of 7 time points was selected for

analysis, but only time points T2 and T5 were used for the analysis here. The cell distance was computed similarly to the Sepal example (Fig. 2D) as distance from the organ base (“Mesh/Heat Map/Location/Cell Distance”; see also user guide chapter 23.1 “The cell distance measure”). Additionally we computed the heat map gradient of the cell distance heat map (“Mesh/Cell Axis/Custom/Create Heatmap Directions”; see user guide chapter 16.2 “Custom direction using a distance heat map”) to obtain custom direction along the proximal distal (PD) axis and orthogonal to that the medial-lateral (ML) axis of the organ for each cell. PDGs were computed and used to determine the amount of growth along the previously computed PD and ML-axis (see user guide chapter 15 “Principal Directions of Growth (PDGs)” and chapter 16 “Custom axis directions”).

For the morphing animation in Figure 6-figure supplement 1A we used T2 and T5 and followed the user guide chapter 17.4 “Morphing Animations”.

For the cell network analysis in Figure 8J-K we computed the cell connectivity network of all cells in T5 weighted by the inverse of the length of the cell walls to determine the betweenness centrality. This is done by running the process “Mesh/Heat Map/Measures/Network/Betweenness Centrality” (Jackson et al., 2019).

Tomato Shoot Apical Meristem (Fig 3F-I)

For the growth and DR5 signal analysis on the shoot apical meristem we used one replicate of the previously published data of (Kierzkowski et al., 2012). To objectively find the center of the meristem, the primoridium, and the initiation site, the curvature of the cells was computed (“Mesh/Cell Axis/Curvature/Compute Tissue Curvature”). The resulting heat map was smoothed across neighboring cells for two rounds and resulting local maxima were identified as centers (“Mesh/Heat Map/Heat Map Smooth”). Meshes were manually aligned along the x-axis with respect to the meristem center to compute circumferential coordinates (“Mesh/Heat Map/Measures/Location/Polar Coord”; see also user guide chapter 23.3 “Further types of organ coordinates”) around the primordium and initiation center. For the analysis only cells in the vicinity of the primordium and initiation centers were considered (as obtained by the cell distance towards their center cell using “Mesh/Heat Map/Measures/Location/Cell Distance”; see also user guide chapter 23.1 “The cell distance measure”). Furthermore, the gradients of the Euclidean cell distance heat maps from both centers were used to compute custom

directions along the heat (=radial) and orthogonal to the heat (=circumferential) (using the process “Mesh/Cell Axis/Custom/Create Heatmap Directions”; see also user guide chapter 16.2 “Custom directions using a distance heat map”). Finally the growth analysis was done similarly to the leaf, computing PDGs and growth along the custom axis (“Mesh/Cell Axis/PDG/Compute Growth Directions”; see also user guide chapter 15 “Principal Directions of Growth (PDGs)” and chapter 16 “Custom axis directions”).

After each step heat maps were exported to attribute maps and in the end exported to csv files (see also chapter 12 “Attribute maps & data export”).

Arabidopsis Gynoecium (Fig 4E-H)

We selected one replicate for further analysis. After the surface segmentation (see user guide chapters 5-9), we computed the heat map for the length of the minor axis in Fig. 4E (process “Mesh/Heat Map/Measures/Geometry/Length Minor Axis”; see also user guide chapter 10 “Cell geometry quantification” and chapter 22 “Cell shape analysis using PCA”). For Fig. 4F, after a manual alignment we computed the x-coordinate of the cells (process “Mesh/Heat Map/Measures/Location/Cell Coordinate”; see also user guide chapter 23.3 “Further types of organ coordinates”). For both of these heat maps, cell types were generated by determining an appropriate threshold and selecting cells by their heat value using the process “Mesh/Heat Map/Heat Map Select” to set their parent label (=cell type label). For more details see also user guide chapter 24.3 “Cell type classification using a single heat map”.

In Figure 4G we created a clustering using the process “Mesh/Cell Types/Classification/Tools/Cell Property Map 2D”. See also the user guide chapter 24.5 “Cell type classification using two measures”.

In Fig. 4H we used the SVM training and classification pipeline to generate the cell type labels from a small training set (as shown in the figure). See also the user guide chapter 24.6 “Cell type classification using SVMs.

Arabidopsis Leaf (Fig 6B-C)

We selected one replicate for segmentation, parent-labeling and the demonstration of the semi-automatic parent labeling. See user guide chapters 5-9 about creating a surface segmentation and chapter 17.2 “Semi-automatic parent labeling” for more details.

Arabidopsis Shoot Apical Meristems (Fig 8L,M, 8S2E,F)

For the MT analysis we selected one sample for segmentation and analysis. We determined the center of organ based on a smoothed curvature heat map (“Mesh/Cell Axis/Curvature/Compute Tissue Curvature”). The center cell was selected and the Euclidean cell distance to the remaining cells was computed (“Mesh/Heat Map/Location/Cell Distance”). The circumferential direction around the cell center was obtained from the orthogonal direction of the heat map directions (“Mesh/Cell Axis/Custom/Create Heatmap Directions”). Cells were then binned by their Euclidean distance to the center (“Mesh/Heat Map/Operators/Heat Map Binning”).

Arabidopsis Embryo (Fig 8F,G, 8S1B-E)

The data for the 3D division analysis in *A. thaliana* embryos was previously published in (Yoshida et al., 2014). From this data set we chose one wild-type and one inducible bdl (pRPS5a>>bdl) sample at the 16 cell stage.

A surface mesh was generated from the cells in the embryo and the cells were parent labeled according to their predicted mother cell. Then the process “Mesh/Division Analysis/Analysis 3D/Division Analysis Multi” performed the following steps on all of the parent labelled cells (n=16 cells or 8 divisions in each genotype): First a planar approximation of the actual division plane was computed by performing a PCA on the vertex positions of the shared wall between the two daughter cells. Then 1000 equally distributed division planes were simulated on the combined mother cell and different measures were quantified. See also the user guide chapter 25.2 “Division Analysis 3D” for more details. The actual and the best planes were visualized using the process “Mesh/Division Analysis/Display and Filter Planes”.

Arabidopsis Root PIN2 in 3D (Fig 8N, 8S2A,B)

For the analysis of the PIN directions in the *A. thaliana* root we selected one sample for 3D segmentation (see user guide chapter 20 “3D segmentation”). Next, we defined the main organ axis using a Bezier curve through the center of the organ (“Mesh/Cell Axis 3D/Custom/Create Bezier Line Directions”; see also user guide chapter 21.6 “Custom directions for 3D meshes”). Then we computed the PIN2 polarity direction (“Mesh/Cell Axis 3D/Polarization/Compute Signal Orientation”; see also user guide chapter 21.7 “Signal orientation for 3D meshes”) and determined the angle between the polarity direction and the Bezier line (“Mesh/Cell Axis 3D/Compute Angles”).

Acknowledgments

We acknowledge support by the Center for Advanced Light Microscopy of the Technical University of Munich School of Life Sciences, and inspiration from the many collaborators we have worked with during the development of MorphoGraphX. We would also like to thank the reviewers and the editor for their helpful comments and suggestions.

Table 1: Measures for cells segmented on surface projections (2.5D).

Measure	Unit	Description
Geometry		
Area	um2	Area of the Cell (sum of its triangle area)
Aspect Ratio	-	Ratio of Length Major Axis and Length Minor Axis (see below)
Average Radius	um	Average distance from the center of gravity of a cell to its border
Junction Distance	um	Max or min distance between neighboring junctions of a cell
Length Major Axis	um	Length of the major axis of the 2D Shape Analysis: (Computes a PCA on the triangle positions weighted by their area)
Length Minor Axis	um	Length of the minor axis of the 2D Shape Analysis: (Computes a PCA on the triangle positions weighted by their area)
Maximum Radius	um	Maximum distance from the cell center to its border
Minimum Radius	um	Minimum distance from the cell center to its border
Perimeter	um	Sum of the length of the border segments of a cell
Lobeyness		
Circularity	-	Perimeter^2/(4*PI*Area)
Lobeyness	-	Ratio of cell perimeter to convex hull perimeter. 1 for convex shapes
Rectangularity	-	Ratio of cell area to the area of the smallest rectangle that can contain the cell. 1 for rectangular shapes, lower values for irregular shapes.
Soldarity	-	Ratio of the convex hull area to the cell area. 1 for convex shapes, higher values for complicated shapes.
Visibility Pavement	-	Simply 1-(Visibility Stomata) (see below)
Visibility Stomata	-	Estimate of visibility in the cell. 1 for convex shapes, decreases with the complexity of the contour.
Location		
Bezier Coord	um	Associated Bezier coordinate of a cell. Requires a Bezier grid.
Bezier Line Coord	um	Associated Bezier coordinate of a cell. Requires a Bezier curve.
Cell Coordinate	um	Cartesian coordinate of a cell
Cell Distance	um/ cells	Distance to the nearest selected cell (finds the shortest path to a selected cell, different distance measures: euclidean, cell number or 1/wall area)
Distance to Bezier	um	Euclidean distance to the Bezier curve or grid
Distance to Mesh	um	Euclidean distance to the nearest vertex in the other mesh
Major Axis Theta	°	Angle between the long axis of the cell and a reference direction
Polar Coord	°/um	Polar coordinate around a specified Cartesian axis
Network		

Neighbors	count	Number of neighbors of a cell
Betweenness Centrality	-	Computes the betweenness centrality of the cell connectivity graph. Edges can be weighted by the length of the shared wall between neighboring cells
Betweenness Current Flow	-	Computes the betweenness current flow of the cell connectivity graph. Edges can be weighted by the length of the shared wall between neighboring cells
Signal		
Signal Border		Average amount of border signal in a cell
Signal Interior		Average amount of interior signal in a cell
Signal Parameters		Advanced and general process which allows the setting of parameters to compute different kinds of signal quantifications
Signal Total		Average amount of total (=border + interior) signal in a cell
Other Measure processes		
Mesh/Lineage Tracking/Heat Map Proliferation	cells	Proliferation
Mesh/Cell Axis/Custom/Custom Direction Angle	°	Angle between a Cell Axis and a Custom Axis
Mesh/Division Analysis/Compute Division Plane Angles	°	Angle between division planes and/or cell axes

Table 2: Measures for meshes with volumetric (3D) cells.

Measure	Unit	Description
Cell Atlas		
Cell Length (Circumferential, Radial, Longitudinal)	um	Cell length as determined by 3D Cell Atlas Root (Shoot rays from the cell center to the side walls to measure cell size along organ-centric directions)
Coord (Circumferential, Radial, Longitudinal)		3D organ coordinates as determined by 3D Cell Atlas Root
Geometry		
Cell Length (Custom, X, Y, Z)	um	Cell length along the specified direction (cell size is measured as in 3D Cell Atlas Root (see above))
Cell Wall Area	um2	Total area of the cell wall
Cell Volume	um3	Volume of the cell
Outside Wall Area	um2	Cell wall area that is not shared with another neighboring cell
Outside Wall Area Ratio	%	Proportion of Cell Wall Area that is not shared with a neighbor cell
Location		
Bezier Coord	um	Associated Bezier coordinate of a cell. Requires a Bezier curve or grid.
Cell Coordinate	um	Cartesian coordinate of a cell
Cell Distance	um/ cells	Distance to the nearest selected cell (finds the shortest path to a selected cell, different distance measures: euclidean, cell number or 1/wall area)
Distance to Bezier	um	Euclidean distance to the Bezier curve or grid
Mesh Distance	um	Euclidean distance to the nearest vertex in the other mesh
Network		
Neighbors	count	Number of neighbors of a cell
Betweenness Centrality	-	Computes the betweenness centrality of the cell connectivity graph. Edges can be weighted by the length of the shared wall between neighboring cells
Betweenness Current Flow	-	Computes the betweenness current flow of the cell connectivity graph. Edges can be weighted by the length of the shared wall between neighboring cells

Table 3. MorphoGraphX workflows.

Workflow	**Description**	**Used in Figure**	**User guide chapter**
MorphoGraphX legacy workflows	Processes and pipelines introduced in MorphoGraphX 1.0 (Barbier de Reuille et al., 2015)		
Surface segmentation	Creating a surface mesh, projecting epidermal signal and segmentation	1A-C	The chapters at the beginning of the user guide deal with these basic topics: from chapter 1 “Introduction” to 12 “Attribute maps & data export”
3D segmentation	Creating volumetric segmentation using ITK watershed	1S1A-B	20 “3D segmentation”
Parent labelling	Cell lineage tracing between two subsequent segmented time points of the same sample	1D,E	13 “Lineage tracking”
Cell geometry heatmaps	Creating heat map of cellular data	1D, 1S1C	10 “Cell geometry quantification”
Time-lapse heat maps	Creating heat maps using two parent labelled time points	1E	14 “Comparing data from two time points”
Growth directions	Computing growth directions using time-lapse data	1E	15 “Principal directions of growth (PDGs)”
MorphoGraphX 2 workflows	New processes and pipelines introduced in this paper		
Different methods of creating organ coordinates	Using world coordinates (X, Y, Z)	2A	23.3 “Further types of organ coordinates”
	Using polar coordinates	3G-I	23.3 “Further types of organ coordinates”

	Using Bezier line or grid	2C	23.2 “Bezier line and grid”
	Using Cell Distance heat maps	2D	23.1 “The cell distance measure”
	Using a separate organ surface mesh	3A	23.3 “Further types of organ coordinates”
Different methods of creating cell type labellings	Using heat maps or organ coordinates	4E-F	24.3 “Cell type classification using a single heat map”
	Using 2D clustering	4G	24.5 “Cell type classification using two measures”
	Using support vector machines (SVMs)	4H	24.6 “Cell type classification using SVMs”
Organ directions	Deriving directions from coordinates or Bezier curves	3B,H	16 “Custom axis directions” & 21.6 “Custom directions for 3D meshes”
Combining directions	Combining different kind of organ coordinates or directions	4B, 5D-F	24.1 “Cell Atlas Root” & 21.6 “Custom Directions for 3D meshes”
Semi-automatic parent labelling	For lineage tracing	6A-C	17.2 “Semi-automatic parent labeling”
Morphing animations		6S1A,B	17.4 “Morphing animations”
3D growth analysis		7D-I	21.3 “Change Maps 3D” & 21.4 “PDGs 3D”
Division analysis	Analyzing cell divisions	8A-I, 8S1A,E	25 “Division analysis”
Cell connectivity analysis	Analyzing cellular connectivity networks	8J,K	-
3D visualization	Exploded views	8S1C	21.5 “3D visualization

			options”
Signal quantification	Quantifying signal amount and direction	8L-N, 8S2A-F	18 “Quantifying signal orientation” & 21.7 “Signal orientation for 3D meshes”

Video Captions

Video 1. Creation of a simple organ-centric coordinate system and its application on cellular data. Starting with two time points of an Arabidopsis sepal that have been lineage traced, the principal directions of growth are computed. Next, cells at the base of the sepal are selected to create a distance field which is used as a simple coordinate system. The growth (areal extension) can then be computed along the directions defined along the organ-centric coordinate system. The organ coordinates can also be exported and used to plot different kinds of cellular data.

Video 2. Cell type classification using Support Vector Machines (SVMs). A selection of measures is calculated on a segmented mesh from an Arabidopsis gynoecium. A sampling of cells are then are labeled by hand, and used as training data. The cell type for the rest of the cells is then predicted automatically.

Video 3. Semi-automatic cell lineage tracking. A few cells from two time points from a time lapse of Marchantia are matched by hand. The other cells can then be determined automatically. trouble spots can be overcome by selecting a few more cells by hand and continuing the process.

Video 4. Animating time lapse data with deformation functions. A time lapse of Marchantia is used to demonstrate how deformation functions can be used to animate growth. Cells are colored by areal growth rate.

Video 5. Creating an animation. Key frames are saved and used to provide steps for an animation which can then be played back.

Video 6. CNN cell wall prediction and segmentation. Using an Arabidopsis flower meristem, a convolution neural network (CNN) is first used to improve the cell wall signal. The mersitem is then segmented into cells, and a 3D mesh created.

Video 7. Calling R from MorphoGraphX. A time lapse of an Arabidopsis leaf is used to demonstrate how to create heat map data for analysis and plotting in R.

References

Aegerter-Wilmsen, T., Heimlicher, M. B., Smith, A. C., de Reuille, P. B., Smith, R. S., Aegerter, C. M., & Basler, K. (2012). Integrating force-sensing and signaling pathways in a model for the regulation of wing imaginal disc size. *Development*, *139*(17), 3221–3231. https://doi.org/10.1242/DEV.082800

Andersen, T. G., Naseer, S., Ursache, R., Wybouw, B., Smet, W., De Rybel, B., Vermeer, J. E. M., & Geldner, N. (2018). Diffusible repression of cytokinin signalling produces endodermal symmetry and passage cells. *Nature*, *555*(7697), 529–533. https://doi.org/10.1038/nature25976

Armour, W. J., Barton, D. A., Law, A. M. K., & Overall, R. L. (2015). Differential Growth in Periclinal and Anticlinal Walls during Lobe Formation in Arabidopsis Cotyledon Pavement Cells. *The Plant Cell*, *27*(9), 2484–2500. https://doi.org/10.1105/tpc.114.126664

Barbier de Reuille, P., Routier-Kierzkowska, A. L., Kierzkowski, D., Bassel, G. W., Schüpbach, T., Tauriello, G., Bajpai, N., Strauss, S., Weber, A., Kiss, A., Burian, A., Hofhuis, H., Sapala, A., Lipowczan, M., Heimlicher, M. B., Robinson, S., Bayer, E. M., Basler, K., Koumoutsakos, P., … Smith, R. S. (2015). MorphoGraphX: A platform for quantifying morphogenesis in 4D. *ELife*, *4*(MAY), 1–20. https://doi.org/10.7554/eLife.05864

Barkoulas, M., Hay, A., Kougioumoutzi, E., & Tsiantis, M. (2008). A developmental framework for dissected leaf formation in the Arabidopsis relative Cardamine hirsuta. *Nature Genetics*, *40*(9), 1136–1141. https://doi.org/10.1038/ng.189

Bartschat, A., Hübner, E., Reischl, M., Mikut, R., & Stegmaier, J. (2016). XPIWIT—an XML pipeline wrapper for the Insight Toolkit. *Bioinformatics*, *32*(2), 315–317. https://doi.org/10.1093/bioinformatics/btv559

Benková, E., Michniewicz, M., Sauer, M., Teichmann, T., Seifertová, D., Jürgens, G., & Friml, J. (2003). Local, Efflux-Dependent Auxin Gradients as a

Common Module for Plant Organ Formation. *Cell*, *115*(5), 591–602. https://doi.org/https://doi.org/10.1016/S0092-8674(03)00924-3

Berg, S., Kutra, D., Kroeger, T., Straehle, C. N., Kausler, B. X., Haubold, C., Schiegg, M., Ales, J., Beier, T., Rudy, M., Eren, K., Cervantes, J. I., Xu, B., Beuttenmueller, F., Wolny, A., Zhang, C., Koethe, U., Hamprecht, F. A., & Kreshuk, A. (2019). ilastik: interactive machine learning for (bio)image analysis. *Nature Methods*, *16*(12), 1226–1232. https://doi.org/10.1038/s41592-019-0582-9

Besson, S., & Dumais, J. (2011). Universal rule for the symmetric division of plant cells. *Proceedings of the National Academy of Sciences of the United States of America*, *108*(15), 6294–6299. https://doi.org/10.1073/pnas.1011866108

Bézier, P. (1968). Procédé de définition numérique des courbes et surfaces non mathématiques. *Automatisme*, *13*(5), 189–196.

Boudaoud, A., Burian, A., Borowska-Wykręt, D., Uyttewaal, M., Wrzalik, R., Kwiatkowska, D., & Hamant, O. (2014). FibrilTool, an ImageJ plug-in to quantify fibrillar structures in raw microscopy images. *Nature Protocols*, *9*(2), 457–463. https://doi.org/10.1038/nprot.2014.024

Bringmann, M., & Bergmann, D. C. (2017). Tissue-wide Mechanical Forces Influence the Polarity of Stomatal Stem Cells in Arabidopsis. *Current Biology*, *27*(6), 877–883. https://doi.org/https://doi.org/10.1016/j.cub.2017.01.059

Catmull, E., & Rom, R. (1974). *A CLASS OF LOCAL INTERPOLATING SPLINES*. 317–326. https://doi.org/10.1016/B978-0-12-079050-0.50020-5

Chang, C.-C., & Lin, C.-J. (2011). LIBSVM: A library for support vector machines. *ACM Transactions on Intelligent Systems and Technology (TIST)*, *2*(3), 27. https://doi.org/10.1145/1961189.1961199

Çiçek, Ö., Abdulkadir, A., Lienkamp, S. S., Brox, T., & Ronneberger, O. (2016). *3D U-Net: Learning Dense Volumetric Segmentation from Sparse Annotation BT - Medical Image Computing and Computer-Assisted Intervention –*

MICCAI 2016 (S. Ourselin, L. Joskowicz, M. R. Sabuncu, G. Unal, & W. Wells (eds.); pp. 424–432). Springer International Publishing.

Cortes, C., & Vapnik, V. (1995). Support-vector networks. *Machine Learning 1995 20:3*, *20*(3), 273–297. https://doi.org/10.1007/BF00994018

de Reuille, P. B., & Ragni, L. (2017). *Vascular Morphodynamics During Secondary Growth BT - Xylem: Methods and Protocols* (M. de Lucas & J. P. Etchhells (eds.); pp. 103–125). Springer New York. https://doi.org/10.1007/978-1-4939-6722-3_10

Duchon, J. (1977). *Splines minimizing rotation-invariant semi-norms in Sobolev spaces BT - Constructive Theory of Functions of Several Variables* (W. Schempp & K. Zeller (eds.); pp. 85–100). Springer Berlin Heidelberg.

Eldridge, T., Łangowski, Ł., Stacey, N., Jantzen, F., Moubayidin, L., Sicard, A., Southam, P., Kennaway, R., Lenhard, M., Coen, E. S., & Østergaard, L. (2016). Fruit shape diversity in the Brassicaceae is generated by varying patterns of anisotropy. *Development*, *143*(18), 3394–3406. https://doi.org/10.1242/DEV.135327

Elsner, J., Lipowczan, M., & Kwiatkowska, D. (2018). Differential growth of pavement cells of Arabidopsis thaliana leaf epidermis as revealed by microbead labeling. *American Journal of Botany*, *105*(2), 257–265. https://doi.org/10.1002/AJB2.1021

Eschweiler, D., Smith, R. S., & Stegmaier, J. (2021). *Robust 3D Cell Segmentation: Extending the View of Cellpose*. https://doi.org/10.48550/arxiv.2105.00794

Eschweiler, D., Spina, T. V, Choudhury, R. C., Meyerowitz, E., Cunha, A., & Stegmaier, J. (2019). CNN-Based Preprocessing to Optimize Watershed-Based Cell Segmentation in 3D Confocal Microscopy Images. *2019 IEEE 16th International Symposium on Biomedical Imaging (ISBI 2019)*, 223–227. https://doi.org/10.1109/ISBI.2019.8759242

Feng, W., Kita, D., Peaucelle, A., Cartwright, H. N., Doan, V., Duan, Q., Liu, M.-C., Maman, J., Steinhorst, L., Schmitz-Thom, I., Yvon, R., Kudla, J., Wu, H.-M., Cheung, A. Y., & Dinneny, J. R. (2018). The FERONIA Receptor Kinase Maintains Cell-Wall Integrity during Salt Stress through Ca2+ Signaling. *Current Biology*, *28*(5), 666-675.e5. https://doi.org/https://doi.org/10.1016/j.cub.2018.01.023

Fernandez, R., Das, P., Mirabet, V., Moscardi, E., Traas, J., Verdeil, J.-L., Malandain, G., & Godin, C. (2010). Imaging plant growth in 4D: robust tissue reconstruction and lineaging at cell resolution. *Nature Methods*, *7*(7), 547–553. https://doi.org/10.1038/nmeth.1472

Fridman, Y., Strauss, S., Horev, G., Ackerman-Lavert, M., Reiner-Benaim, A., Lane, B., Smith, R. S., & Savaldi-Goldstein, S. (2021). The root meristem is shaped by brassinosteroid control of cell geometry. *Nature Plants*, *7*(11), 1475–1484. https://doi.org/10.1038/s41477-021-01014-9

Green, A. A., Kennaway, J. R., Hanna, A. I., Bangham, J. A., & Coen, E. (2010). Genetic Control of Organ Shape and Tissue Polarity. *PLOS Biology*, *8*(11), e1000537. https://doi.org/10.1371/journal.pbio.1000537

Hejnowicz, Z. (1984). Trajectories of principal directions of growth, natural coordinate system in growing plant organ. In *Acta Societatis Botanicorum Poloniae* (Vol. 53, Issue 1, pp. 29–42). https://doi.org/10.5586/asbp.1984.004

Hervieux, N., Dumond, M., Sapala, A., Routier-Kierzkowska, A.-L., Kierzkowski, D., Roeder, A. H. K., Smith, R. S., Boudaoud, A., & Hamant, O. (2016). A Mechanical Feedback Restricts Sepal Growth and Shape in Arabidopsis. *Current Biology*, *26*(8), 1019–1028. https://doi.org/https://doi.org/10.1016/j.cub.2016.03.004

Hong, L., Dumond, M., Tsugawa, S., Sapala, A., Routier-Kierzkowska, A.-L., Zhou, Y., Chen, C., Kiss, A., Zhu, M., Hamant, O., Smith, R. S., Komatsuzaki, T., Li, C.-B., Boudaoud, A., & Roeder, A. H. K. (2016). Variable Cell Growth Yields Reproducible Organ Development through Spatiotemporal Averaging.

Developmental Cell, *38*(1), 15–32. https://doi.org/https://doi.org/10.1016/j.devcel.2016.06.016

Jackson, M. D. B., Duran-Nebreda, S., Kierzkowski, D., Strauss, S., Xu, H., Landrein, B., Hamant, O., Smith, R. S., Johnston, I. G., & Bassel, G. W. (2019). Global Topological Order Emerges through Local Mechanical Control of Cell Divisions in the Arabidopsis Shoot Apical Meristem. *Cell Systems*, *8*(1), 53-65.e3. https://doi.org/https://doi.org/10.1016/j.cels.2018.12.009

Jackson, M. D. B., Xu, H., Duran-Nebreda, S., Stamm, P., & Bassel, G. W. (2017). Topological analysis of multicellular complexity in the plant hypocotyl. *ELife*, *6*. https://doi.org/10.7554/ELIFE.26023

Kennaway, R., & Coen, E. (2019). Volumetric finite-element modelling of biological growth. *Open Biology*, *9*(5). https://doi.org/10.1098/RSOB.190057

Kierzkowski, D., Nakayama, N., Routier-Kierzkowska, A.-L., Weber, A., Bayer, E., Schorderet, M., Reinhardt, D., Kuhlemeier, C., & Smith, R. S. (2012). Elastic Domains Regulate Growth and Organogenesis in the Plant Shoot Apical Meristem. *Science*, *335*(6072), 1096 LP – 1099. https://doi.org/10.1126/science.1213100

Kierzkowski, D., Runions, A., Vuolo, F., Strauss, S., Lymbouridou, R., Routier-Kierzkowska, A.-L., Wilson-Sánchez, D., Jenke, H., Galinha, C., Mosca, G., Zhang, Z., Canales, C., Dello Ioio, R., Huijser, P., Smith, R. S., & Tsiantis, M. (2019). A Growth-Based Framework for Leaf Shape Development and Diversity. *Cell*, *177*(6), 1405-1418.e17. https://doi.org/https://doi.org/10.1016/j.cell.2019.05.011

Kuchen, E. E., Fox, S., Barbier de Reuille, P., Kennaway, R., Bensmihen, S., Avondo, J., Calder, G. M., Southam, P., Robinson, S., Bangham, A., & Coen, E. (2012). Generation of Leaf Shape Through Early Patterns of Growth and Tissue Polarity. *Science*, *335*(6072), 1092 LP – 1096. https://doi.org/10.1126/science.1214678

Li, W., Agrawala, M., Curless, B., & Salesin, D. (2008). Automated generation of interactive 3D exploded view diagrams. *ACM Transactions on Graphics (TOG)*, *27*(3). https://doi.org/10.1145/1360612.1360700

Linkert, M., Rueden, C. T., Allan, C., Burel, J.-M., Moore, W., Patterson, A., Loranger, B., Moore, J., Neves, C., MacDonald, D., Tarkowska, A., Sticco, C., Hill, E., Rossner, M., Eliceiri, K. W., & Swedlow, J. R. (2010). Metadata matters: access to image data in the real world. *Journal of Cell Biology*, *189*(5), 777–782. https://doi.org/10.1083/jcb.201004104

Liu, S., Strauss, S., Adibi, M., Mosca, G., Yoshida, S., Dello Ioio, R., Runions, A., Andersen, T. G., Grossmann, G., Huijser, P., Smith, R. S., & Tsiantis, M. (2022). Cytokinin promotes growth cessation in the Arabidopsis root. *Current Biology*. https://doi.org/https://doi.org/10.1016/j.cub.2022.03.019

Louveaux, M., Julien, J.-D., Mirabet, V., Boudaoud, A., & Hamant, O. (2016). Cell division plane orientation based on tensile stress in Arabidopsis thaliana. *Proceedings of the National Academy of Sciences of the United States of America*, *113*(30), E4294-303. https://doi.org/10.1073/pnas.1600677113

Marhava, P., Hoermayer, L., Yoshida, S., Marhavý, P., Benková, E., & Friml, J. (2019). Re-activation of Stem Cell Pathways for Pattern Restoration in Plant Wound Healing. *Cell*, *177*(4), 957-969.e13. https://doi.org/https://doi.org/10.1016/j.cell.2019.04.015

Montenegro-Johnson, T., Stamm, P., Strauss, S., Topham, A. T., Tsagris, M., Wood, A. T. A., Smith, R. S., & Bassel, G. W. (2015). Digital Single-Cell Analysis of Plant Organ Development Using 3DCellAtlas. *The Plant Cell*, *27*(4), 1018–1033. https://doi.org/10.1105/tpc.15.00175

Montenegro-Johnson, T., Strauss, S., Jackson, M. D. B., Walker, L., Smith, R. S., & Bassel, G. W. (2019). 3DCellAtlas Meristem: a tool for the global cellular annotation of shoot apical meristems. *Plant Methods 2019 15:1*, *15*(1), 1–9. https://doi.org/10.1186/S13007-019-0413-0

Reinhardt, D., Pesce, E.-R., Stieger, P., Mandel, T., Baltensperger, K., Bennett, M., Traas, J., Friml, J., & Kuhlemeier, C. (2003). Regulation of phyllotaxis by polar auxin transport. *Nature*, *426*(6964), 255–260. https://doi.org/10.1038/nature02081

Ripoll, J.-J., Zhu, M., Brocke, S., Hon, C. T., Yanofsky, M. F., Boudaoud, A., & Roeder, A. H. K. (2019). Growth dynamics of the Arabidopsis fruit is mediated by cell expansion. *Proceedings of the National Academy of Sciences*, *116*(50), 25333–25342. https://doi.org/10.1073/PNAS.1914096116

Sankar, M., Nieminen, K., Ragni, L., Xenarios, I., & Hardtke, C. S. (2014). Automated quantitative histology reveals vascular morphodynamics during Arabidopsis hypocotyl secondary growth. *ELife*, *2014*(3). https://doi.org/10.7554/ELIFE.01567

Sapala, A., Runions, A., Routier-Kierzkowska, A. L., Gupta, M. Das, Hong, L., Hofhuis, H., Verger, S., Mosca, G., Li, C. B., Hay, A., Hamant, O., Roeder, A. H. K., Tsiantis, M., Prusinkiewicz, P., & Smith, R. S. (2018). Why plants make puzzle cells, and how their shape emerges. *ELife*, *7*. https://doi.org/10.7554/ELIFE.32794

Scheres, B., Benfey, P., & Dolan, L. (2002). Root development. *The Arabidopsis Book*, *1*, e0101–e0101. https://doi.org/10.1199/tab.0101

Scheuring, D., Löfke, C., Krüger, F., Kittelmann, M., Eisa, A., Hughes, L., Smith, R. S., Hawes, C., Schumacher, K., & Kleine-Vehn, J. (2016). Actin-dependent vacuolar occupancy of the cell determines auxin-induced growth repression. *Proceedings of the National Academy of Sciences*, *113*(2), 452–457. https://doi.org/10.1073/PNAS.1517445113

Schindelin, J., Arganda-Carreras, I., Frise, E., Kaynig, V., Longair, M., Pietzsch, T., Preibisch, S., Rueden, C., Saalfeld, S., Schmid, B., Tinevez, J.-Y., White, D. J., Hartenstein, V., Eliceiri, K., Tomancak, P., & Cardona, A. (2012). Fiji: an open-source platform for biological-image analysis. *Nature Methods*, *9*(7), 676–682. https://doi.org/10.1038/nmeth.2019

Schmidt, T., Pasternak, T., Liu, K., Blein, T., Aubry-Hivet, D., Dovzhenko, A., Duerr, J., Teale, W., Ditengou, F. A., Burkhardt, H., Ronneberger, O., & Palme, K. (2014). The iRoCS Toolbox – 3D analysis of the plant root apical meristem at cellular resolution. *The Plant Journal*, *77*(5), 806–814. https://doi.org/10.1111/TPJ.12429

Schneitz, K., Hülskamp, M., & Pruitt, R. E. (1995). Wild-type ovule development in Arabidopsis thaliana: a light microscope study of cleared whole-mount tissue. *The Plant Journal*, *7*(5), 731–749. https://doi.org/10.1046/J.1365-313X.1995.07050731.X

Segonzac, C., Nimchuk, Z. L., Beck, M., Tarr, P. T., Robatzek, S., Meyerowitz, E. M., & Zipfel, C. (2012). The Shoot Apical Meristem Regulatory Peptide CLV3 Does Not Activate Innate Immunity. *The Plant Cell*, *24*(8), 3186–3192. https://doi.org/10.1105/tpc.111.091264

Silveira, S. R., Le Gloanec, C., Gómez-Felipe, A., Routier-Kierzkowska, A.-L., & Kierzkowski, D. (2022). Live-imaging provides an atlas of cellular growth dynamics in the stamen. *Plant Physiology*, *188*(2), 769–781. https://doi.org/10.1093/plphys/kiab363

Smith, R. S., Guyomarc'h, S., Mandel, T., Reinhardt, D., Kuhlemeier, C., & Prusinkiewicz, P. (2006). A plausible model of phyllotaxis. *Proceedings of the National Academy of Sciences of the United States of America*, *103*(5), 1301–1306. https://doi.org/10.1073/pnas.0510457103

Sommer, C., Straehle, C., Köthe, U., & Hamprecht, F. A. (2011). Ilastik: Interactive learning and segmentation toolkit. *2011 IEEE International Symposium on Biomedical Imaging: From Nano to Macro*, 230–233. https://doi.org/10.1109/ISBI.2011.5872394

Stamm, P., Strauss, S., Montenegro-Johnson, T. D., Smith, R., & Bassel, G. W. (2017). *In Silico Methods for Cell Annotation, Quantification of Gene Expression, and Cell Geometry at Single-Cell Resolution Using 3DCellAtlas BT - Plant Hormones: Methods and Protocols* (J. Kleine-Vehn & M. Sauer

(eds.); pp. 99–123). Springer New York. https://doi.org/10.1007/978-1-4939-6469-7_11

Stegmaier, J., Amat, F., Lemon, W. C., McDole, K., Wan, Y., Teodoro, G., Mikut, R., & Keller, P. J. (2016). Real-Time Three-Dimensional Cell Segmentation in Large-Scale Microscopy Data of Developing Embryos. *Developmental Cell*, *36*(2), 225–240. https://doi.org/https://doi.org/10.1016/j.devcel.2015.12.028

Stegmaier, J., Otte, J. C., Kobitski, A., Bartschat, A., Garcia, A., Nienhaus, G. U., Strähle, U., & Mikut, R. (2014). Fast Segmentation of Stained Nuclei in Terabyte-Scale, Time Resolved 3D Microscopy Image Stacks. *PLOS ONE*, *9*(2), e90036. https://doi.org/10.1371/JOURNAL.PONE.0090036

Strauss, S., Sapala, A., Kierzkowski, D., & Smith, R. S. (2019). *Quantifying Plant Growth and Cell Proliferation with MorphoGraphX BT - Plant Cell Morphogenesis: Methods and Protocols* (F. Cvrčková & V. Žárský (eds.); pp. 269–290). Springer New York. https://doi.org/10.1007/978-1-4939-9469-4_18

Thompson, D. W. (1942). *On growth and form*. Cambridge University Press.

Tsugawa, S., Hervieux, N., Kierzkowski, D., Routier-Kierzkowska, A.-L., Sapala, A., Hamant, O., Smith, R. S., Roeder, A. H. K., Boudaoud, A., & Li, C.-B. (2017). Clones of cells switch from reduction to enhancement of size variability in Arabidopsis sepals. *Development*, *144*(23), 4398–4405. https://doi.org/10.1242/DEV.153999

Turk, G., & O'Brien, J. F. (1999). *Variational implicit surfaces*. Georgia Institute of Technology.

Van Bruaene, N., Joss, G., & Van Oostveldt, P. (2004). Reorganization and in Vivo Dynamics of Microtubules during Arabidopsis Root Hair Development. *Plant Physiology*, *136*(4), 3905–3919. https://doi.org/10.1104/pp.103.031591

van den Berg, C., Willemsen, V., Hage, W., Weisbeek, P., & Scheres, B. (1995). Cell fate in the Arabidopsis root meristem determined by directional signalling. *Nature*, *378*(6552), 62–65. https://doi.org/10.1038/378062a0

Vijayan, A., Strauss, S., Tofanelli, R., Mody, T. A., Lee, K., Tsiantis, M., Smith, R. S., & Schneitz, K. (2022). The annotation and analysis of complex 3D plant organs using 3DCoordX. *Plant Physiology*, kiac145. https://doi.org/10.1093/plphys/kiac145

Vijayan, A., Tofanelli, R., Strauss, S., Cerrone, L., Wolny, A., Strohmeier, J., Kreshuk, A., Hamprecht, F. A., Smith, R. S., & Schneitz, K. (2021). A digital 3D reference atlas reveals cellular growth patterns shaping the arabidopsis ovule. *ELife*, *10*, 1–38. https://doi.org/10.7554/ELIFE.63262

Vlad, D., Kierzkowski, D., Rast, M. I., Vuolo, F., Ioio, R. Dello, Galinha, C., Gan, X., Hajheidari, M., Hay, A., Smith, R. S., Huijser, P., Bailey, C. D., & Tsiantis, M. (2014). Leaf Shape Evolution Through Duplication, Regulatory Diversification, and Loss of a Homeobox Gene. *Science*, *780*(February), 780–783. https://doi.org/10.1126/science.1248384

Whitewoods, C. D., Gonçalves, B., Cheng, J., Cui, M., Kennaway, R., Lee, K., Bushell, C., Yu, M., Piao, C., & Coen, E. (2020). Evolution of carnivorous traps from planar leaves through simple shifts in gene expression. *Science*, *367*(6473), 91 LP – 96. https://doi.org/10.1126/science.aay5433

Willis, L., Refahi, Y., Wightman, R., Landrein, B., Teles, J., Huang, K. C., Meyerowitz, E. M., & Jönsson, H. (2016). Cell size and growth regulation in the Arabidopsis thaliana apical stem cell niche. *Proceedings of the National Academy of Sciences of the United States of America*, *113*(51), E8238–E8246. https://doi.org/10.1073/PNAS.1616768113

Wolny, A., Cerrone, L., Vijayan, A., Tofanelli, R., Barro, A. V., Louveaux, M., Wenzl, C., Strauss, S., Wilson-Sánchez, D., Lymbouridou, R., Steigleder, S. S., Pape, C., Bailoni, A., Duran-Nebreda, S., Bassel, G., Lohmann, J. U., Tsiantis, M., Hamprecht, F. A., Schneitz, K., … Kreshuk, A. (2020). Accurate and versatile 3D segmentation of plant tissues at cellular resolution. *ELife*, *9*, 1–34. https://doi.org/10.7554/ELIFE.57613

Wolpert, L. (1969). Positional information and the spatial pattern of cellular differentiation. *Journal of Theoretical Biology*, *25*(1), 1–47. https://doi.org/https://doi.org/10.1016/S0022-5193(69)80016-0

Xu, J., & Scheres, B. (2005). Dissection of Arabidopsis ADP-RIBOSYLATION FACTOR 1 Function in Epidermal Cell Polarity. *The Plant Cell*, *17*(2), 525–536. https://doi.org/10.1105/tpc.104.028449

Yoshida, S., Barbier de Reuille, P., Lane, B., Bassel, G. W., Prusinkiewicz, P., Smith, R. S., & Weijers, D. (2014). Genetic Control of Plant Development by Overriding a Geometric Division Rule. *Developmental Cell*, *29*(1), 75–87. https://doi.org/https://doi.org/10.1016/j.devcel.2014.02.002

Zhang, Z., Runions, A., Mentink, R. A., Kierzkowski, D., Karady, M., Hashemi, B., Huijser, P., Strauss, S., Gan, X., Ljung, K., & Tsiantis, M. (2020). A WOX/Auxin Biosynthesis Module Controls Growth to Shape Leaf Form. *Current Biology*, *30*(24), 4857-4868.e6. https://doi.org/https://doi.org/10.1016/j.cub.2020.09.037

Zhu, M., Chen, W., Mirabet, V., Hong, L., Bovio, S., Strauss, S., Schwarz, E. M., Tsugawa, S., Wang, Z., Smith, R. S., Li, C.-B., Hamant, O., Boudaoud, A., & Roeder, A. H. K. (2020). Robust organ size requires robust timing of initiation orchestrated by focused auxin and cytokinin signalling. *Nature Plants*, *6*(6), 686–698. https://doi.org/10.1038/s41477-020-0666-7